International Journal of Mechanical Sciences 248 (2023) 108160

Contents lists available at ScienceDirect

International Journal of Mechanical Sciences

journal homepage: www.elsevier.com/locate/ijmecsci

Quasi-static crack propagation in soft materials using the material-sink theory

Suhib Abu-Qbeitah, Mahmood Jabareen *, Konstantin Y. Volokh

Faculty of Civil and Environmental Engineering, Structural Engineering and Construction Management Division, Technion - Israel Institute of Technology, Haifa 32000, Israel

ARTICLE INFO

Keywords:
Material-sink model
Reduced mixed finite-element
Quasi-static fracture
Brittle fracture
Hyperelasticity

ABSTRACT

In the present study, a finite element formulation for the material-sink approach aimed at modeling quasi-static crack propagation in hyperelastic solids is developed. Breakage of molecular bonds leads to material separation and appearance of two new surfaces of a crack. However, the bond breakage is diffusive, and the loss of local bonds leads to the localized material (molecular) loss. The latter notion triggers consideration of mass density as a variable that numerically decreases in the area where damage localizes into a crack. This physical notion requires mathematical consideration of mass balance as an additional and active law, which regularizes the computational model. From the numerical point of view, the developed finite element formulation has displacement and density degrees of freedom. Also, a monolithic approach was applied that ensures stable incrimination of the nonlinear problem. Numerical examples of the fracture of aneurysm material demonstrate the high robustness of the proposed approach.

1. Introduction

One hundred years ago Griffith proposed a theory of brittle fracture [1] in which an energy criterion for instability of pre-existing cracks was defined. This pioneering work initiated new field of research called fracture mechanics [2]. Based on the Griffith theory, the linear elastic fracture mechanics and its generalizations [3] were developed to account for nonlinear phenomena associated with the crack instability. Years after the Griffith work, computers revolutionized the field of fracture mechanics allowing for analyzing the instability of pre-existing cracks as well as modeling the whole process of fracture including the crack nucleation, propagation, branching, and arrest. Roughly speaking, computer methods can be categorized into two groups: surface or discrete and bulk or diffusive.

Surface models are characterized by inserting cracks of zero thickness in the form of displacement discontinuities and specifying their traction–separation constitutive laws [4–16]. Such models have been successfully implemented to simulate cracks along existing material interfaces. If the weak interface is not known in advance then cohesive surfaces are inserted at the edges of the finite elements. However, a drawback of curbing the crack to propagate only along element edges is that the fracture energy is overestimated when the true crack path deviates significantly from the corresponding element edge, particularly when the mesh is coarse [17]. In addition, the use of two different constitutive laws for the bulk and internal surfaces induces artificial material anisotropy.

To circumvent the latter dependence of the crack propagation on the element boundaries, the embedded discontinuity finite element method (ED-FEM) has been proposed, where as its name suggests the localization zone is embedded at the element level [18]. It is a discrete crack approach where displacement field is enhanced with supplementary kinematics to capture displacement jumps in a single element [19]. The ED-FEM can use relatively coarse mesh and can be used to avoid repeated remeshing that is required in traditional discrete crack approaches leading to mesh-independent results [20]. However, tracking algorithms used within the ED-FEM approach can be computationally demanding especially in solving complex crack propagation such as branching in dynamic fracture [19]. The extended finite element method (XFEM) [11,21] is considered as a possible alternative to the above-mentioned approach since it uses the element enrichment via a partition of unity framework. Such element enrichment enables cracks to propagate independently of the underlying mesh. It also resolves the stress singularities issue at the crack tip as well as it models the true stress behavior at the tip vicinity using coarser mesh compared to the case without enrichment. Nonetheless, XFEM suffers from the computational complexity with the increase of the number of individual crack segments and additional degrees of freedom [17].

* Corresponding author.
E-mail address: cvjmah@technion.ac.il (M. Jabareen).

https://doi.org/10.1016/j.ijmecsci.2023.108160
Received 17 July 2022; Received in revised form 28 December 2022; Accepted 19 January 2023
Available online 10 February 2023

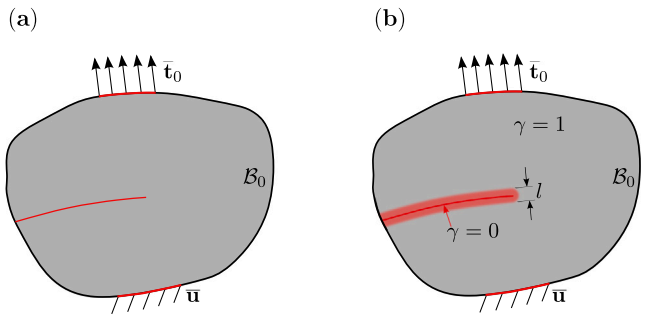

Fig. 1. Material-sink regularization of (a) sharp crack discontinuity into (b) diffusive representation by the relative mass density γ. The characteristic length l controls the width of the regularized fracture zone.

Bulk models describe cracks having finite rather than zero thickness and obeying bulk constitutive laws with falling stress–strain curves [22–29]. In this case, crack nucleation, propagation, and arrest naturally come out of the theory. However, bulk models are not spared from shortcomings as well. They suffer from the localization of deformation into narrow bands exhibiting dependence on the size of the computational mesh. In the limit case where the element size approaches a very small value, damage takes place while illogically dissipating zero energy. The latter shortcoming led to the emergence of nonlocal continuum formulations [30–34]. In the recent years, especially popular became the so-called phase-field methods [35–47]. These methods are based on the introduction of an auxiliary scalar field called phase-field variable establishing the connection between the broken and unbroken states of material. Physical interpretations of the phase fields and equations defining them are far from being obvious. Such physical difficulties are intrinsic in most nonlocal formulations, which are based on the tacit assumptions of the long-range atomic interactions. Actual atomic interactions are short range — on the angstrom scale. It is not uncommon also to see claims in the literature that some phase-field formulations allow for convergence of the diffused cracks to the zero-thickness Griffith cracks under the decrease of the thickness of the diffused area. Unfortunately, these claims are open to discussion because the characteristic thickness is not a freely changing number but rather a physical parameter related to the material strength.

While most diffused bulk models of crack modeling lean on the purely mathematical regularization techniques, Volokh [48] proposed the so-called material-sink (MS) approach rooted in physics of the fracture process. The central point of the MS approach is the physical observation that broken bonds are diffused rather than confined to two neighbor atomic layers. Diffused broken bonds unavoidably lead to the local loss of material — debris, sometimes observable via naked eye. Thus, mass is not conserved within small areas of the crack localization and the mass balance equation should be coupled with the momenta balance. Naturally, the mass density, rather than damage or phase-field variables, becomes the additional variable, which together with mass balance law provides regularization of crack simulations. Remarkably, the MS formulation reduces to hyperelasticity with energy limiters [49–54] prior the material failure localizes into cracks. Due to its mathematical simplicity and physical transparency, the MS model can be flexibly implemented in various finite element codes and commercial programs. For example, it has been recently implemented in FEAP software to study the inertia effect in dynamic failure processes [55].

In the present work, a modified version of the material sink (MS) approach for modeling quasi-static crack propagation in soft materials is developed. Such modification substantially enhances the numerical solution and extends the capabilities of the method in modeling fracture in brittle materials. Specifically, the MS theory is used to study the failure mechanisms of an abdominal aortic aneurysm material undergoing large deformation gaining new insights into its mechanical behavior and design. Also, the MS approach is examined through a number of benchmark two-dimensional and three-dimensional examples to demonstrate the feasibility and effectiveness of the current approach in predicting complex crack patterns including branching, bridging and crack propagation along curved geometries. In particular, the MS approach is implemented as a user-defined element (UEL) in the commercial software package Abaqus/Standard 2020 [56] and the detailed numerical implementation of the coupled mass-deformation theory is discussed.

The paper is organized as follows: Section 2 provides details of the material-sink fracture model employed herein and the constitutive equations used for numerical simulations. Section 3 presents the finite-element methodology adopted in this work, in particular, a reduced mixed formulation. The implementation in Abaqus is discussed in Section 4 and the numerical simulations of benchmark problems are presented in Section 5. Finally, Section 6 summarizes the present study.

2. Theoretical background of the material-sink approach at finite deformation

The basic idea of the material-sink is that the bond breakage appears as a result of the development of multiple micro-cracks leading to localized loss of mass. The latter implies replacing conservation of mass by the mass balance presenting the mass density as the damage variable that approaches a value of zero in the cracked areas. In this section, a brief summary of the material-sink (MS) formulation is introduced. Interested readers are referred to the original formulation proposed by Volokh [48] for additional details about the MS theory.

In the context of continuum mechanics, consider a material point occupying a position $\mathbf{X}$ in the domain $\mathcal{B}_0$ at the reference configuration of a deformable body, which moves to position $\mathbf{x}$ in the domain $\mathcal{B}$ at the current configuration. Deformation in the vicinity of the material point is described by the deformation gradient $\mathbf{F} = \partial\mathbf{x}/\partial\mathbf{X}$ that maps the reference configuration to the current one with the constraint $J = \det\mathbf{F} > 0$. It should be noted that the Lagrangian or material description is adopted in the present work.

2.1. Balance equations

As already mentioned, the material-sink postulates the mathematical consideration of the mass balance as an additional and active law coupled with momenta balance, where crack initiation, propagation, branching, etc. are all embedded in the PDEs. Following [48], the mass balance takes the form

$$\frac{d\rho}{dt} = \mathrm{Div}\,(\mathbf{s}) + \xi = 0, \tag{1}$$

where ρ is the referential mass density, $\mathbf{s}$ is the referential mass flux, and ξ is the referential mass source/sink, and $\mathrm{Div}\,(\bullet)$ is the divergence operator defined with respect to the referential coordinates.

It is assumed that failure and mass sink are highly localized and, consequently, momenta and energy balance equations can be written in the standard forms. Thus, the momenta balance equations are as follows

$$\mathrm{Div}\,(\mathbf{FS}) + \rho\mathbf{b} = \mathbf{0}, \quad \mathbf{S} = \mathbf{S}^{\mathrm{T}}, \tag{2}$$

where $\mathbf{b}$ is the referential mechanical body forces per unit mass and $\mathbf{S}$ is the second Piola–Kirchhoff stress tensor.

To complete the formulation of the boundary value problem, proper boundary conditions need to be specified. The mechanical and mass Neumann boundary conditions are, respectively, given by

$$\begin{aligned} &\mathbf{FSN} = \bar{\mathbf{t}}_0, \\ &\mathbf{s}\cdot\mathbf{N} = 0, \end{aligned} \tag{3}$$

where $\mathbf{N}$ is the unit outward normal to the boundary in the reference configuration, $\bar{\mathbf{t}}_0$ is the external mechanical traction applied on the

boundary $\partial\mathcal{B}_0^{\mathbf{t}_0}$. It should be noted that ((3)b) implies that there is no mass flux out of the boundary $\partial\mathcal{B}_0^{\mathbf{s}}$. Alternatively, the Dirichlet boundary conditions are defined by prescribing displacement (i.e. $\mathbf{u}=\bar{\mathbf{u}}$ on $\partial\mathcal{B}_0^{u}$) and mass density (i.e. $\rho=\bar{\rho}$ on $\partial\mathcal{B}_0^{\rho}$). Fig. 1a illustrates the prescribed mechanical natural and essential boundary conditions on a solid body. In particular, Fig. 1a shows the undeformed body occupied by the domain $\mathcal{B}_0$ and subjected to the traction $\bar{\mathbf{t}}_0$ on the boundary $\partial\mathcal{B}_0^{\mathbf{t}_0}$. Also, the domain incorporates a sharp crack discontinuity that represents discrete crack. Such representation will be regularized into a diffusive one as will be discussed in the next subsection.

2.2. Constitutive equations

Here, the constitutive equation for the second Piola–Kirchhoff stress tensor, which is derived directly from thermodynamic considerations [48], is as follows

$$\mathbf{S}=2\rho\frac{\partial w}{\partial\mathbf{C}}, \tag{4}$$

where w is the specific Helmholtz free energy function per unit mass and $\mathbf{C}=\mathbf{F}^{\mathrm{T}}\mathbf{F}$ is the right Cauchy–Green deformation tensor.

Next, the constitutive law for the mass source/sink can be defined in the following form [48]

$$\xi=\beta\rho_0-\frac{\beta\rho}{H(\alpha)\,\mathrm{e}^{-(w/\phi)^m}}, \tag{5}$$

where $\rho_0=\rho(t=0)$ is the initial referential mass density, $\beta>0$ is a material constant, ϕ is the specific energy limiter per unit mass, and m is a dimensionless material parameter, which controls the sharpness of the transition to material failure on the stress–strain curve. Also, $H(\alpha)$ is a unit step function (i.e. $H(\alpha)=0$ if $\alpha<0$ and $H(\alpha)=1$ otherwise), and the switch parameter $\alpha\in(-\infty;0\,]$ is necessary to prevent material healing process. Following [55], the switch parameter can be defined by the evolution equation $\dot{\alpha}=-H\left(\epsilon-\rho/\rho_0\right)$, where $0<\epsilon\ll 1$ is a precision constant.

The constitutive law for the Lagrangian mass flux can be written by analogy with the Fourier law for heat conduction as follows

$$\mathbf{s}=\kappa\mathrm{Grad}\,(\rho)\,, \tag{6}$$

where $\kappa>0$ is a mass conductivity for the isotropic case. It should be noted that the constitutive equations for the mass source (5) and flux (6) are modified as compared to the original form given in [48]. Such modification facilitates the numerical solution. The new version of the mass flux implies that the diffusion is isotropic in the initial configuration, after deformation, internal bonds are reoriented and their distribution is not isotropic. Evidently, (6) implies that the diffusion of broken bonds is isotropic with respect to the reference configuration.

Now, substitution of (5) and (6) in (1) and dividing by $\beta\rho_0$ yields

$$\mathrm{Div}\,(\mathbf{f})+\zeta=0, \tag{7}$$

where the vector $\mathbf{f}$ and the scalar ζ are defined as follows

$$\begin{aligned}\mathbf{f}&=l^2\mathrm{Grad}\,(\gamma)\,,\\ \zeta&=1-\frac{\gamma}{H(\alpha)\,\mathrm{e}^{-(W/\Phi)^m}+\varepsilon},\end{aligned} \tag{8}$$

in which $0<\varepsilon\ll 1$ is a dimensionless constant that serves to avoid numerical singularity when H approaches zero. From the numerical point of view, the constant ε was set to 10^{-11} (i.e. $\varepsilon=10^{-11}$). The parameter $l=\sqrt{\kappa/\beta}$ is the characteristic length of the material. It is noticed from (8) that the scalars κ and β are not required as the characteristic length replaces them. Also, the dimensionless (or relative) mass density γ, the Helmholtz free energy per unit referential volume W and the energy limiter (or the average bond energy) per unit referential volume Φ are defined as follows

$$\gamma=\frac{\rho}{\rho_0},\quad W=\rho_0 w,\quad \Phi=\rho_0\phi. \tag{9}$$

It is worth mentioning that since the characteristic length (also referred to as the regularization parameter) is a small parameter providing the dimensional consistency of the equation, solutions of the boundary layer type that represent the diffused crack can be obtained. In other words, the characteristic length l controls the width of the regularized fracture zone wherein the relative density has values ranging from 0 to 1, corresponding respectively to fully broken (i.e. $\gamma=0$) and intact states (i.e. $\gamma=1$). Thus, the relative mass density approaches 0 inside a regularized crack and approaches 1 far away from the fracture surface. Within Fig. 1 the described regularization scheme for the fracture problem by means of the introduced length scale parameter is illustrated, where the discrete crack surface in Fig. 1a is regularized into a diffusive crack representation as in Fig. 1b via the relative mass density field γ. It should be noted that the length scale is considered a material parameter that can be calibrated via experimental data. Moreover, the length scale has a physical meaning that the bond breakage is not confined to two adjacent molecular layers, and the process involves thousands of layers within an area or volume with the representative characteristic size l.

Now, using ((9)a) and ((9)b), the constitutive equations for the second Piola–Kirchhoff stress can be expressed as follows

$$\mathbf{S}=\gamma\mathbf{S}_0,\quad \mathbf{S}_0=2\frac{\partial W}{\partial\mathbf{C}}, \tag{10}$$

where $\mathbf{S}_0$ is the second Piola–Kirchhoff stress tensor of the virgin material.

Next, for later consideration, the linearized forms of the second Piola–Kirchhoff stress tensor $\mathbf{S}$, the vector $\mathbf{f}$, and the scalar ζ are given by

$$\begin{aligned}\Delta\mathbf{S}&=\frac{\partial\mathbf{S}}{\partial\mathbf{C}}:\Delta\mathbf{C}+\frac{\partial\mathbf{S}}{\partial\gamma}\Delta\gamma=\mathbb{C}_{uu}:\frac{1}{2}\Delta\mathbf{C}+\mathbf{C}_{u\gamma}\Delta\gamma,\\ \Delta\mathbf{f}&=\frac{\partial\mathbf{f}}{\partial\left(\mathrm{Grad}\,(\gamma)\right)}\cdot\mathrm{Grad}\,(\Delta\gamma)=\mathbf{C}_{\gamma\gamma}\cdot\mathrm{Grad}\,(\Delta\gamma)\,,\\ \Delta\zeta&=\frac{\partial\zeta}{\partial\mathbf{C}}:\Delta\mathbf{C}+\frac{\partial\zeta}{\partial\gamma}\Delta\gamma=\mathbf{C}_{\gamma u}:\frac{1}{2}\Delta\mathbf{C}+\mathrm{C}_{\gamma\gamma}\Delta\gamma,\end{aligned} \tag{11}$$

where the fourth-order tensor $\mathbb{C}_{uu}$ is defined by

$$\mathbb{C}_{uu}=2\frac{\partial\mathbf{S}}{\partial\mathbf{C}}=\gamma\mathbb{C}_{uu0},\quad \mathbb{C}_{uu0}=4\frac{\partial^2 W}{\partial\mathbf{C}\partial\mathbf{C}}, \tag{12}$$

and the second-order tensors $\mathbf{C}_{u\gamma}$ and $\mathbf{C}_{\gamma u}$ take the following forms

$$\begin{aligned}\mathbf{C}_{u\gamma}&=\frac{\partial\mathbf{S}}{\partial\gamma}=\mathbf{S}_0,\\ \mathbf{C}_{\gamma u}&=2\frac{\partial\zeta}{\partial\mathbf{C}}=-\frac{H(\alpha)\,\mathrm{e}^{-(W/\Phi)^m}\frac{m}{\Phi}\left(\frac{W}{\Phi}\right)^{m-1}}{\left(H(\alpha)\,\mathrm{e}^{-(W/\Phi)^m}+\varepsilon\right)^2}\mathbf{S},\end{aligned} \tag{13}$$

and both the second-order tensor $\mathbf{C}_{\gamma\gamma}$ and the scalar $\mathrm{C}_{\gamma\gamma}$ are defined by

$$\begin{aligned}\mathbf{C}_{\gamma\gamma}&=\frac{\partial\mathbf{f}}{\partial\left(\mathrm{Grad}\,(\gamma)\right)}=l^2\mathbf{I},\\ \mathrm{C}_{\gamma\gamma}&=\frac{\partial\zeta}{\partial\gamma}=-\frac{1}{H(\alpha)\,\mathrm{e}^{-(W/\Phi)^m}+\varepsilon}.\end{aligned} \tag{14}$$

Without loss of generality, the strain energy function per unit referential volume $W=W(\mathbf{C})$ can be additively split into two terms

$$W=W_{\mathrm{vol.}}(J)+W_{\mathrm{dis.}}\left(I_1'\right), \tag{15}$$

where the first term controls the volumetric deformation and the second one controls the distortional deformation. Also, $I_1'=J^{-2/3}\mathbf{C}:\mathbf{I}$ is the first invariant of the distortional part of the deformation tensor $\mathbf{C}$ (i.e. $\mathbf{C}_{\mathrm{dis.}}=J^{-2/3}\mathbf{C}$). Substituting (15) into ((10)b) and ((12)b) to deduce the expressions for the second Piola–Kirchhoff stress and the material tangent modulus of the virgin material, respectively

$$\begin{aligned}\mathbf{S}_0&=J\frac{\partial W_{\mathrm{vol.}}}{\partial J}\mathbf{C}^{-1}\\ &\quad+2\frac{\partial W_{\mathrm{dis.}}}{\partial I_1'}\left(J^{-2/3}\mathbf{I}-\frac{1}{3}I_1'\mathbf{C}^{-1}\right),\end{aligned}$$

$$
\begin{aligned}
\mathbb{C}_{uu0} = {} & J\frac{\partial}{\partial J}\left(J\frac{\partial W_{\text{vol.}}}{\partial J}\right)\mathbf{C}^{-1}\otimes\mathbf{C}^{-1} \\
& + 2J\frac{\partial W_{\text{vol.}}}{\partial J}\frac{\partial \mathbf{C}^{-1}}{\partial \mathbf{C}} + 4J^{-4/3}\frac{\partial^2 W_{\text{dis.}}}{\partial I_1'\partial I_1'}\mathbf{I}\otimes\mathbf{I} \\
& - \frac{4}{3}J^{-2/3}\frac{\partial}{\partial I_1'}\left(I_1'\frac{\partial W_{\text{dis.}}}{\partial I_1'}\right)\mathbf{I}\otimes\mathbf{C}^{-1} \\
& - \frac{4}{3}J^{-2/3}\frac{\partial}{\partial I_1'}\left(I_1'\frac{\partial W_{\text{dis.}}}{\partial I_1'}\right)\mathbf{C}^{-1}\otimes\mathbf{I} \\
& + \frac{4}{9}I_1'\frac{\partial}{\partial I_1'}\left(I_1'\frac{\partial W_{\text{dis.}}}{\partial I_1'}\right)\mathbf{C}^{-1}\otimes\mathbf{C}^{-1} \\
& - \frac{4}{3}I_1'\frac{\partial W_{\text{dis.}}}{\partial I_1'}\frac{\partial \mathbf{C}^{-1}}{\partial \mathbf{C}}.
\end{aligned}
\tag{16}
$$

The specific choice of the constitutive law for the mass source (5) is a subtle matter and we explain it as follows. Let us consider the onset of material damage – failure – prior the damage localizes into cracks. In the latter case, the mass flux vanishes (i.e. $\mathbf{s}=\mathbf{0}$). Then using the mass balance equation, the mass source term should also vanish (i.e. $\xi=0$), and thus, it implies that the unknown dimensionless mass density is given by

$$
\gamma = H(\alpha)\,\mathrm{e}^{-(W/\Phi)^m}. \tag{17}
$$

Since the irreversibility of the process is not important prior damage localizes into crack, the step function H can be dropped out from (17) to obtain

$$
\gamma = \mathrm{e}^{-(W/\Phi)^m}. \tag{18}
$$

Then, substituting of (18) in (10) yields

$$
\mathbf{S} = 2\mathrm{e}^{-(W/\Phi)^m}\frac{\partial W}{\partial \mathbf{C}}. \tag{19}
$$

In the case of hyperelastic material, a strain energy function is postulated $\psi(\mathbf{C})$, which satisfies the following condition

$$
\frac{\partial \psi}{\partial \mathbf{C}} = \mathrm{e}^{-(W/\Phi)^m}\frac{\partial W}{\partial \mathbf{C}}. \tag{20}
$$

Such energy function exists, indeed, and it can be written in the following form

$$
\psi(\mathbf{C}) = \psi_{\text{f}} - \psi_{\text{e}}(\mathbf{C}), \tag{21}
$$

where $\psi_e(\mathbf{C})$ is the elastic energy defined by

$$
\psi_{\text{e}}(\mathbf{C}) = \frac{\Phi}{m}\Gamma\left[\frac{1}{m},\left(\frac{W(\mathbf{C})}{\Phi}\right)^m\right], \tag{22}
$$

and $\psi_{\text{f}} = \psi_{\text{e}}(\mathbf{I})$ is the failure energy. In (22), $\Gamma[s,x] = \int_x^\infty t^{s-1}e^{-t}dt$ is the upper incomplete gamma function.

The strain energy in (21) is bounded! Specifically, the bounded strain energy is a direct expression of the physical fact that the number of particles in a material volume is bounded as well as the energy of their bonds. Also, the bounded strain energy automatically provides bounded stresses indicating material instability and failure. The reader is referred to works [49,50,54,57] concerning the theory and implications of hyperelasticity with energy limiters — the bounded strain energy.

3. Finite-element formulation

Classical finite element approach exhibits volumetric locking behavior when modeling nearly incompressible materials (e.g. soft materials). To overcome this deficiency, the point-wise dilatation measure is replaced by an average one, whereas the distortional part remains valid point-wise. Therefore, the modified deformation tensor which is motivated by the multiplicative split of the deformation gradient into volumetric part and isochoric part can be defined as follows

$$
\overline{\mathbf{C}} = \underbrace{\overline{J}^{2/3}\mathbf{I}}_{\overline{\mathbf{C}}_{\text{vol.}}}\underbrace{J^{-2/3}\mathbf{C}}_{\overline{\mathbf{C}}_{\text{dis.}}} = \left(\frac{\overline{J}}{J}\right)^{2/3}\mathbf{C}, \tag{23}
$$

where $\overline{J}$ is the assumed dilatation measure. Using the work by Jabareen [58], Bishara and Jabareen [59], a reduced mixed finite-element formulation with two fields for the coupled problem is derived instead of the four field formulation. Specifically, the four independent fields are the modified deformation tensor, an assumed dilatation measure, an assumed hydrostatic pressure, and the relative mass density. Thus, the Hu–Washizu functional of the coupled problem can be written with respect to the four fields, where the variation of the functional with respect to the different fields yields variational equations. Following [58,59], it can be shown that the penalty term in the functional of the total potential energy vanishes due to the assumption that both the assumed dilatation measure and assumed hydrostatic pressure are constants at the element level together with implying the solution of the variational equation obtained by the variation with respect to the assumed hydrostatic pressure. By doing so, the functional of the total potential energy reduces to be function of the two fields — the modified deformation tensor and the relative mass density. In particular, the solution of the variational equation derived from the variation of the functional of the total potential energy with respect to the assumed hydrostatic pressure is given by

$$
\overline{J} = \frac{1}{\Omega_0^{\text{e}}}\int_{\Omega_0^{\text{e}}} J\,d\Omega_0^{\text{e}}. \tag{24}
$$

According to (24), the assumed dilatation measure is interpreted as the volume average of the point-wise dilatation, and it is denoted as the average volumetric deformation. Also, Ω_0^{e} in (24) is the element referential volume. It should be noted that when postulating (24), the average volumetric deformation is no longer an independent field. Now, the weak form of the coupled problem is given by $\delta\Pi = \sum_{e=1}^{N_{el}}\delta\Pi^e = 0$, in which $\delta\Pi^e$ is expressed by

$$
\begin{aligned}
\delta\Pi^{\text{e}} = {} & \int_{\Omega_0^{\text{e}}}\left(\overline{\mathbf{S}}:\delta\overline{\mathbf{E}} + \mathbf{f}\cdot\text{Grad}\,(\delta\gamma) - \overline{\zeta}\delta\gamma\right)d\Omega_0^{\text{e}} \\
& - \int_{\partial B_0^{t_0}}\overline{\mathbf{t}}\cdot\delta\mathbf{u}\,d\Gamma_0,
\end{aligned}
\tag{25}
$$

where $\left\{\overline{\mathbf{S}},\overline{\mathbf{E}},\overline{\zeta}\right\}$ are modified quantities evaluated using the modified right Cauchy–Green deformation tensor (23) and the average volumetric deformation (24).

Next, the variation of the modified Green–Lagrange strain tensor ($\overline{\mathbf{E}} = \left(\overline{\mathbf{C}}-\mathbf{I}\right)/2$) is expressed in terms of the variation of the modified deformation tensor as follows

$$
\delta\overline{\mathbf{E}} = \frac{1}{2}\delta\overline{\mathbf{C}} = \frac{1}{2}\left(\frac{\overline{J}}{J}\right)^{2/3}\delta\mathbf{C} + \frac{1}{3}\left(\frac{\delta\overline{J}}{\overline{J}} - \frac{\delta J}{J}\right)\overline{\mathbf{C}}. \tag{26}
$$

Using the relationship between the volume change and the right Cauchy–Green deformation tensor and using (24), the variation of both the dilatation and the volume average of the dilatation are obtained by

$$
\delta J = \frac{1}{2}J\mathbf{C}^{-1}:\delta\mathbf{C}, \quad \delta\overline{J} = \frac{1}{\Omega_0^{\text{e}}}\int_{\Omega_0^{\text{e}}}\delta J\,d\Omega_0^{\text{e}}. \tag{27}
$$

For deriving the tangent stiffness, a linearization of the variation (25) is required, which is given by

$$
\begin{aligned}
\Delta\delta\Pi^{\text{e}} = {} & \int_{\Omega_0^{\text{e}}}\Big(\delta\overline{\mathbf{E}}:\overline{\mathbb{C}}_{uu}:\Delta\overline{\mathbf{E}} + \overline{\mathbf{S}}:\Delta\delta\overline{\mathbf{E}} \\
& + \delta\overline{\mathbf{E}}:\overline{\mathbf{C}}_{u\gamma}\Delta\gamma - \delta\gamma\overline{\mathbf{C}}_{\gamma u}:\Delta\overline{\mathbf{E}} - \delta\gamma\overline{\mathbf{C}}_{\gamma\gamma}\Delta\gamma \\
& + \text{Grad}(\delta\gamma)\cdot\mathbf{C}_{\gamma\gamma}\cdot\text{Grad}\,(\Delta\gamma)\Big)\,d\Omega_0^{\text{e}},
\end{aligned}
\tag{28}
$$

where the moduli $\left\{\overline{\mathbb{C}}_{uu}, \overline{\mathbf{C}}_{u\gamma}, \overline{\mathbf{C}}_{\gamma u}, \overline{\mathbb{C}}_{\gamma\gamma}\right\}$ are determined by ((12)a), ((13)a), ((13)b), and ((14)b), where $\left\{\overline{J}, \overline{\mathbf{C}}\right\}$ are used instead of $\{J, \mathbf{C}\}$. The linearization of the variation of the modified Green–Lagrange strain tensor (i.e. $\Delta\delta\overline{\mathbf{E}}$) can be calculated as follows

$$\begin{aligned}\Delta\delta\overline{\mathbf{E}} = {} & \frac{1}{2}\left(\frac{\overline{J}}{J}\right)^{2/3}\Delta\delta\mathbf{C} + \frac{1}{3}\left(\frac{\Delta\overline{J}}{\overline{J}} - \frac{\Delta J}{J}\right)\delta\overline{\mathbf{C}} \\ & + \frac{1}{3}\left(\frac{\delta\overline{J}}{\overline{J}} - \frac{\delta J}{J}\right)\Delta\overline{\mathbf{C}} + \frac{1}{3}\left(\frac{\Delta\delta\overline{J}}{\overline{J}} - \frac{\Delta\delta J}{J}\right. \\ & - \frac{5}{3}\frac{\Delta\overline{J}\delta\overline{J}}{\overline{J}^2} + \frac{1}{3}\frac{\delta J\Delta J}{J^2} + \frac{2}{3}\frac{\Delta J}{J}\frac{\delta\overline{J}}{\overline{J}} \\ & \left. + \frac{2}{3}\frac{\Delta\overline{J}}{\overline{J}}\frac{\delta J}{J}\right)\overline{\mathbf{C}},\end{aligned} \tag{29}$$

where the linearization of the variation of the volume change (i.e. $\Delta\delta J$) and the linearization of the variation of volumetric dilatation (i.e. $\Delta\delta\overline{J}$) are given by

$$\begin{aligned}\Delta\delta J = {} & \frac{1}{4}J\delta\mathbf{C} : \left(\mathbf{C}^{-1}\otimes\mathbf{C}^{-1}\right) : \Delta\mathbf{C} \\ & + \frac{1}{2}J\delta\mathbf{C} : \Delta\mathbf{C}^{-1} + \frac{1}{2}J\mathbf{C}^{-1} : \Delta\delta\mathbf{C}, \\ \Delta\delta\overline{J} = {} & \frac{1}{\Omega_0^{\mathrm{e}}}\int_{\Omega_0^{\mathrm{e}}}\Delta\delta J\, d\Omega_0^{\mathrm{e}}.\end{aligned} \tag{30}$$

Now, within the finite-element methodology, shape functions are used to approximate the primary field variables. In the present study, displacement and relative mass density fields are the primary fields. Therefore, the displacement field, the virtual displacement field, the relative mass density field, and the virtual relative mass density field are interpolated inside each element by

$$\begin{aligned}\mathbf{u} &= \sum_{I=1}^{n_{en}} N_I\hat{\underline{\mathbf{u}}}^I = \underline{\underline{\mathbf{N}}}_u\,\hat{\underline{\mathbf{u}}}, \quad \delta\mathbf{u} = \sum_{I=1}^{n_{en}} N_I\delta\hat{\underline{\mathbf{u}}}^I = \underline{\underline{\mathbf{N}}}_u\,\delta\hat{\underline{\mathbf{u}}}, \\ \gamma &= \sum_{I=1}^{n_{en}} N_I\hat{\gamma}^I = \underline{\mathbf{N}}_\gamma\hat{\underline{\gamma}}, \quad \delta\gamma = \sum_{I=1}^{n_{en}} N_I\delta\hat{\gamma}^I = \underline{\mathbf{N}}_\gamma\delta\hat{\underline{\gamma}},\end{aligned} \tag{31}$$

where $\left\{\hat{\underline{\mathbf{u}}}^I, \delta\hat{\underline{\mathbf{u}}}^I, \hat{\gamma}^I, \delta\hat{\gamma}^I\right\}$ denote the displacement vector, the virtual displacement vector, the relative mass density scalar, and the virtual relative mass density scalar at node I, respectively. Also, n_{en} is the number of the nodes in a single element, and N_I is the shape function for node I.

In this section, a development for a three-dimensional eight-node brick element for which $n_{en} = 8$ is presented. However, the formulation is similarly applicable for two-dimensional and axisymmetric elements, where $n_{en} = 4$. For finite-element development, it is convenient to introduce the following auxiliary vectors

$$\begin{aligned}&\hat{\underline{\mathbf{u}}} = \left\{\hat{\underline{\mathbf{u}}}^1, \hat{\underline{\mathbf{u}}}^2, \ldots, \hat{\underline{\mathbf{u}}}^8\right\}^{\mathrm{T}}, \quad \delta\hat{\underline{\mathbf{u}}} = \left\{\delta\hat{\underline{\mathbf{u}}}^1, \delta\hat{\underline{\mathbf{u}}}^2, \ldots, \delta\hat{\underline{\mathbf{u}}}^8\right\}^{\mathrm{T}}, \\ &\hat{\underline{\gamma}} = \left\{\hat{\gamma}^1, \hat{\gamma}^2, \ldots, \hat{\gamma}^8\right\}^{\mathrm{T}}, \quad \delta\hat{\underline{\gamma}} = \left\{\delta\hat{\gamma}^1, \delta\hat{\gamma}^2, \ldots, \delta\hat{\gamma}^8\right\}^{\mathrm{T}},\end{aligned} \tag{32}$$

which include all nodal displacement vectors, all nodal virtual displacement vectors, all nodal relative mass density scalars, and all nodal virtual relative mass density scalars, respectively. Also, the matrix $\underline{\underline{\mathbf{N}}}_u$ and the row vector $\underline{\mathbf{N}}_\gamma$ are defined by

$$\begin{aligned}\underline{\underline{\mathbf{N}}}_u &= \begin{bmatrix} N_1 & 0 & 0 & \ldots & N_8 & 0 & 0 \\ 0 & N_1 & 0 & \ldots & 0 & N_8 & 0 \\ 0 & 0 & N_1 & \ldots & 0 & 0 & N_8 \end{bmatrix}, \\ \underline{\mathbf{N}}_\gamma &= \begin{Bmatrix} N_1, & N_2, & \ldots & , N_8 \end{Bmatrix}.\end{aligned} \tag{33}$$

In addition, it is convenient to use the matrix notation rather than the tensorial notation for finite element derivations. Specifically, in the matrix notation, vectors and second-order tensors become vectors (indicated by a single underline), while fourth-order tensors become matrices (indicated by a double underline). Following Jabareen [58], Bishara and Jabareen [59] in developing the expression for the variation of the modified Green–Lagrange tensor in terms of the virtual nodal displacements, first the variation of the right Cauchy–Green deformation tensor is written as follows

$$\delta\underline{\mathbf{C}} = 2\sum_{I=1}^{8}\underline{\underline{\mathbf{B}}}_I\,\delta\hat{\underline{\mathbf{u}}}^I = 2\underline{\underline{\mathbf{B}}}_u\,\delta\hat{\underline{\mathbf{u}}}, \tag{34}$$

where the matrix $\underline{\underline{\mathbf{B}}}_u$ is of size 6×24 that contains all $\underline{\underline{\mathbf{B}}}_I$ matrices

$$\underline{\underline{\mathbf{B}}}_u = \begin{bmatrix} \underline{\underline{\mathbf{B}}}_1, & \underline{\underline{\mathbf{B}}}_2, & \ldots & , \underline{\underline{\mathbf{B}}}_8 \end{bmatrix}. \tag{35}$$

In (35), each $\underline{\underline{\mathbf{B}}}_I$ matrix is of size 6×3 and has the following form

$$\underline{\underline{\mathbf{B}}}_I = \begin{bmatrix} F_{11}N_{I,1} & F_{21}N_{I,1} & F_{31}N_{I,1} \\ F_{12}N_{I,2} & F_{22}N_{I,2} & F_{32}N_{I,2} \\ F_{13}N_{I,3} & F_{23}N_{I,3} & F_{33}N_{I,3} \\ F_{11}N_{I,2} + F_{12}N_{I,1} & F_{21}N_{I,2} + F_{22}N_{I,1} & F_{31}N_{I,2} + F_{32}N_{I,1} \\ F_{12}N_{I,3} + F_{13}N_{I,2} & F_{22}N_{I,3} + F_{23}N_{I,2} & F_{32}N_{I,3} + F_{33}N_{I,2} \\ F_{13}N_{I,1} + F_{11}N_{I,3} & F_{23}N_{I,1} + F_{21}N_{I,3} & F_{33}N_{I,1} + F_{31}N_{I,3} \end{bmatrix}, \tag{36}$$

where F_{ij} are the Cartesian components of the deformation gradient tensor and $N_{I,j}$ is the derivative of the shape function of node I with respect to the referential coordinate j (i.e. $N_{I,j} = \partial N_I/\partial X_j$). Substituting of (34) in (27) yields expressions for the variation of the point-wise dilatation and the volume average of the point-wise dilatation in terms of the virtual nodal displacements such as

$$\begin{aligned}\delta J &= \delta\hat{\underline{\mathbf{u}}}^{\mathrm{T}}\underline{\mathbf{a}}_1, \qquad \underline{\mathbf{a}}_1 = J\underline{\underline{\mathbf{B}}}_u^{\mathrm{T}}\underline{\mathbf{C}}^{-1}, \\ \delta\overline{J} &= \delta\hat{\underline{\mathbf{u}}}^{\mathrm{T}}\overline{\underline{\mathbf{a}}}_1, \qquad \overline{\underline{\mathbf{a}}}_1 = \frac{1}{\Omega_0^{\mathrm{e}}}\int_{\Omega_0^{\mathrm{e}}}\underline{\mathbf{a}}_1\, d\Omega_0^{\mathrm{e}},\end{aligned} \tag{37}$$

where $\underline{\mathbf{C}}^{-1}$ is a column vector consisting of the components of the inverse of the right Cauchy–Green deformation tensor, and it is defined as

$$\underline{\mathbf{C}}^{-1} = \left\{C_{11}^{-1}, C_{22}^{-1}, C_{33}^{-1}, C_{12}^{-1}, C_{23}^{-1}, C_{31}^{-1}\right\}^{\mathrm{T}}. \tag{38}$$

The variation of the modified Green–Lagrange strain tensor can be written using the Voigt notation and expressed in terms of the virtual nodal displacements by substituting (34), (37) in (26)

$$\begin{aligned}\delta\overline{\underline{\mathbf{E}}} &= \left\{\delta\overline{E}_{11}, \delta\overline{E}_{22}, \delta\overline{E}_{33}, 2\delta\overline{E}_{12}, 2\delta\overline{E}_{23}, 2\delta\overline{E}_{31}\right\}^{\mathrm{T}} \\ &= \overline{\underline{\underline{\mathbf{B}}}}_u\,\delta\hat{\underline{\mathbf{u}}},\end{aligned} \tag{39}$$

where the matrix $\overline{\underline{\underline{\mathbf{B}}}}_u$ reads

$$\overline{\underline{\underline{\mathbf{B}}}}_u = \left(\frac{\overline{J}}{J}\right)^{2/3}\underline{\underline{\mathbf{B}}}_u + \frac{1}{3}\overline{\mathbf{C}}\left(\frac{\overline{\underline{\mathbf{a}}}_1^{\mathrm{T}}}{\overline{J}} - \frac{\underline{\mathbf{a}}_1^{\mathrm{T}}}{J}\right). \tag{40}$$

Similarly, the variation of the relative density gradient can be written in terms of the virtual nodal relative mass density by substituting for the virtual relative mass density field from ((31)d)

$$\mathrm{Grad}(\delta\gamma) = \underline{\underline{\mathbf{B}}}_\gamma\,\delta\hat{\underline{\gamma}}, \quad \underline{\underline{\mathbf{B}}}_\gamma = \begin{bmatrix} N_{1,1} & N_{2,1} & \ldots & N_{8,1} \\ N_{1,2} & N_{2,2} & \ldots & N_{8,2} \\ N_{1,3} & N_{2,3} & \ldots & N_{8,3} \end{bmatrix}. \tag{41}$$

Now, substituting the developed discretization given in (39), (41), and ((31)d) in (25) yields

$$\delta\Pi^{\mathrm{e}} = \delta\hat{\underline{\mathbf{u}}}^{\mathrm{T}}\left(\hat{\underline{\mathbf{F}}}_u^{\mathrm{int,e}} - \hat{\underline{\mathbf{F}}}_u^{\mathrm{ext,e}}\right) + \delta\hat{\underline{\gamma}}^{\mathrm{T}}\hat{\underline{\mathbf{F}}}_\gamma^{\mathrm{int,e}}, \tag{42}$$

where both the internal and external nodal generalized forces are articulated as

$$\begin{aligned}\hat{\underline{\mathbf{F}}}_u^{\mathrm{int,e}} &= \int_{\Omega_0^{\mathrm{e}}}\overline{\underline{\underline{\mathbf{B}}}}_u^{\mathrm{T}}\overline{\underline{\mathbf{S}}}\, d\Omega_0^{\mathrm{e}}, \quad \hat{\underline{\mathbf{F}}}_u^{\mathrm{ext,e}} = \int_{\partial\mathcal{B}_0^{\mathbf{t}_0}}\underline{\underline{\mathbf{N}}}_u^{\mathrm{T}}\underline{\mathbf{t}}\, d\Gamma_0, \\ \hat{\underline{\mathbf{F}}}_\gamma^{\mathrm{int,e}} &= \int_{\Omega_0^{\mathrm{e}}}\left(\underline{\underline{\mathbf{B}}}_\gamma^{\mathrm{T}}\underline{\mathbf{f}} - \underline{\mathbf{N}}_\gamma^{\mathrm{T}}\overline{\zeta}\right) d\Omega_0^{\mathrm{e}},\end{aligned} \tag{43}$$

and $\underline{\overline{\mathbf{S}}}$ indicates a vector of the entries of the second Piola–Kirchhoff stress tensor, which is defined as

$$\underline{\overline{\mathbf{S}}} = \left\{ \overline{S}_{11}, \overline{S}_{22}, \overline{S}_{33}, \overline{S}_{12}, \overline{S}_{23}, \overline{S}_{31} \right\}^{\mathrm{T}}. \tag{44}$$

In addition, in order to develop the tangent stiffness matrix, a discretization given in (39), (41), ((31)d) are substituted into (28) to deduce

$$\Delta\delta\Pi^{\mathrm{e}} = \left\{ \delta\underline{\hat{\mathbf{u}}}, \delta\underline{\hat{\gamma}} \right\}^{\mathrm{T}} \begin{bmatrix} \underline{\underline{\mathbf{K}}}^{\mathrm{e}}_{uu} & \underline{\underline{\mathbf{K}}}^{\mathrm{e}}_{u\gamma} \\ \underline{\underline{\mathbf{K}}}^{\mathrm{e}}_{\gamma u} & \underline{\underline{\mathbf{K}}}^{\mathrm{e}}_{\gamma\gamma} \end{bmatrix} \begin{bmatrix} \Delta\underline{\hat{\mathbf{u}}} \\ \Delta\underline{\hat{\gamma}} \end{bmatrix}, \tag{45}$$

where $\left\{ \underline{\underline{\mathbf{K}}}^{\mathrm{e}}_{uu}, \underline{\underline{\mathbf{K}}}^{\mathrm{e}}_{\gamma\gamma} \right\}$ are, respectively, the tangent stiffness matrices related to the displacement field and the relative mass density field. In addition, the matrices $\left\{ \underline{\underline{\mathbf{K}}}^{\mathrm{e}}_{u\gamma}, \underline{\underline{\mathbf{K}}}^{\mathrm{e}}_{\gamma u} \right\}$ are related to the coupling between the two fields. The four matrices have the following forms

$$\begin{aligned}
\underline{\underline{\mathbf{K}}}^{\mathrm{e}}_{uu} &= \int_{\Omega^{\mathrm{e}}_0} \left(\underline{\overline{\mathbf{B}}}^{\mathrm{T}}_{u} \underline{\underline{\overline{\mathbf{D}}}}_{uu} \underline{\overline{\mathbf{B}}}_{u} + \underline{\overline{\mathbf{k}}}^{\mathrm{e}}_{G} \right) d\Omega^{\mathrm{e}}_0, \\
\underline{\underline{\mathbf{K}}}^{\mathrm{e}}_{u\gamma} &= \int_{\Omega^{\mathrm{e}}_0} \underline{\overline{\mathbf{B}}}^{\mathrm{T}}_{u} \underline{\underline{\overline{\mathbf{D}}}}_{u\gamma} \underline{\mathbf{N}}_{\gamma} d\Omega^{\mathrm{e}}_0, \\
\underline{\underline{\mathbf{K}}}^{\mathrm{e}}_{\gamma u} &= -\int_{\Omega^{\mathrm{e}}_0} \underline{\mathbf{N}}^{\mathrm{T}}_{\gamma} \underline{\overline{\mathbf{D}}}_{\gamma u} \underline{\overline{\mathbf{B}}}_{u} d\Omega^{\mathrm{e}}_0, \\
\underline{\underline{\mathbf{K}}}^{\mathrm{e}}_{\gamma\gamma} &= \int_{\Omega^{\mathrm{e}}_0} \left(\underline{\mathbf{B}}^{\mathrm{T}}_{\gamma} \underline{\underline{\mathbf{D}}}_{\gamma\gamma} \underline{\mathbf{B}}_{\gamma} - \underline{\mathbf{N}}^{\mathrm{T}}_{\gamma} \overline{\mathrm{D}}_{\gamma\gamma} \underline{\mathbf{N}}_{\gamma} \right) d\Omega^{\mathrm{e}}_0,
\end{aligned} \tag{46}$$

where $\left\{ \underline{\underline{\overline{\mathbf{D}}}}_{uu}, \underline{\underline{\overline{\mathbf{D}}}}_{u\gamma}, \underline{\underline{\overline{\mathbf{D}}}}_{\gamma u}, \underline{\underline{\mathbf{D}}}_{\gamma\gamma} \right\}$ are the matrix forms of the tensors $\left\{ \overline{\mathbb{C}}_{uu}, \overline{\mathbf{C}}_{u\gamma}, \overline{\mathbf{C}}_{\gamma u}, \mathbf{C}_{\gamma\gamma} \right\}$, and $\underline{\overline{\mathbf{k}}}^{\mathrm{e}}_{G}$ is the geometrical tangent stiffness matrix per unit referential volume and it is defined by

$$\underline{\overline{\mathbf{k}}}^{\mathrm{e}}_{G} = \sum_{i=1}^{3} \sum_{j=1}^{3} \overline{S}_{ij} \frac{\partial^2 \Delta\delta \overline{E}_{ij}}{\partial\delta\underline{\hat{\mathbf{u}}} \partial\Delta\underline{\hat{\mathbf{u}}}}. \tag{47}$$

The detailed development of the geometrical tangent stiffness matrix is presented in Appendix A.

4. Abaqus implementation

In the present study, the UEL subroutine is used to implement the MS method. One can imagine the UEL as a box that takes data as inputs, processes them, and then passes the output back to Abaqus. It receives location of nodes at the reference configuration, material parameters from the input file. Also, the updated nodal degrees of freedom including the location of the nodes at the current configuration and the relative mass density are passed in from Abaqus at each iteration of the different increments to calculate the element's residual vector (RHS) and the element's tangent stiffness matrix (AMATRX). The element's vector RHS and the element's matrix AMATRX are updated during the course of analysis and passed back to Abaqus by the UEL. Then, all residuals are assembled into a global residual vector, and all tangent stiffness matrices are assembled into a global stiffness matrix.

It is worth noting that the UEL subroutine is written in FORTRAN language and it contains Gauss points locations, shape functions and their derivatives, kinematic and constitutive relations for calculating the element's residual vector (RHS) and the element's tangent stiffness matrix (AMATRX). Also, the input file can be generated primarily by Abaqus/CAE to depict the geometry and mesh of the desired model, and then it can be modified to be used with the user-elements. For more information on creating Abaqus input files, interested readers are referred to Chester et al. [60], and Jabareen [58].

The coupled system of fracture and large deformation is implemented in Abaqus/Standard by using a coupled temperature–displacement step in the input file, while the user elements have displacements and temperature degrees of freedom for each node.

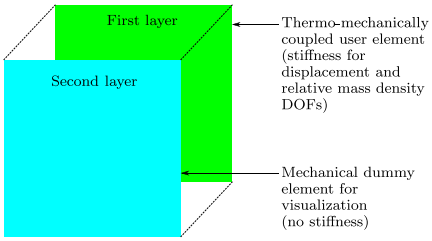

Fig. 2. Representation of two layers finite elements structure in Abaqus. The first layer contributes to the stiffness of both the displacement and temperature (relative mass density) DOFs. For post processing purposes, a second layer overlays the first layer created as a UMAT model.

The latter degree of freedom represents the relative mass density. Concerning implementing the theory in 2D and 3D solids, a two-dimensional four-node element with 3 degrees of freedom at each node (i.e. u_x, u_y and γ) and a three-dimensional eight-node brick element with 4 degrees of freedom at each node (i.e. u_x, u_y, u_z and γ) are respectively defined.

One drawback of using the UEL subroutine is that results of the user-elements cannot be visualized, because the element shape functions are user-defined. One way to circumvent this obstacle is to use a dummy mesh laying over the user-elements mesh (as shown in Fig. 2), which has the same number of nodes and the same number of integration points with negligible elastic modulus to ensure that the dummy mesh will not contribute to the structural response. It is important to note that the dummy elements shall be purely mechanical — that is they do not have a temperature degree of freedom to make sure that their presence will not affect the main problem. Then, the UMAT subroutine is used to transfer the state dependent variables from the user-elements mesh to the overlaying mesh to be visualized through the dummy mesh. As previously noted, the user elements have displacements as well as relative mass density (temperature) DOFs. To make these degrees of freedom available, at least one built-in element must be a thermo-mechanically coupled element. In the case of 2D simulations one element must be of a thermo-mechanically coupled type such as CPE4T, which is not connected to the real model and has a negligibly small elastic modulus.

It should be noted that when crack propagates along element, the element may undergo excessive deformation and becomes highly distorted. In this scenario, the element need to be removed from the calculations as the element fails. Hence, the element deletion controlled by solution-dependent state variables available in Abaqus/Standard 2020 [56] is employed, which is controlled by the user subroutine UMAT. Deleted elements do not carry stresses and do not contribute to the total stiffness of the model [56]. The user shall select which state variable related to element deletion and assign it a value of one or zero. It has a value of one for all material points at the beginning of the analysis. Afterwards, when the deletion criterion is satisfied this flag variable will have a value of zero indicating that this material point is inactive. In Abaqus/Standard (implicit), an element is deleted if the deletion criterion is satisfied at all of its integration points. Specifically, in the present study, when the relative mass densities at all integration points become less than or equal to 10^{-6}, the element is deleted. The status of an element can be determined by requesting the output variable STATUS, where a value of one means the element is active and a zero if the element is deleted.

The displacement and the relative mass density fields in the coupled system can be solved as either sequentially coupled (staggered) or fully coupled (monolithic) fields. In a staggered scheme, the displacement sub-system and the relative mass density sub-system are solved sequentially entailing an alternative minimization approach. On the other hand, in a monolithic approach, the two sub-systems are solved simultaneously. The monolithic solution strategies are unconditionally

stable and, therefore, more efficient (in principle). In the present study, we employ the finite-element software Abaqus to solve the monolithic material-sink model.

Finally, the dissipated energy per unit depth for each failed element (U_i) due to crack propagation is calculated using the failure energy as follows

$$U_i = A_i \psi_f = A_i \Phi m^{-1} \Gamma[m^{-1}, W(\mathbf{I})^m \Phi^{-m}], \tag{48}$$

where A_i is the referential area of the ith failed element.

5. Numerical examples

In this section, standard numerical examples are used to investigate the capabilities of the material-sink approach to capture different aspects of the fracture process in soft materials.

In the following subsections, the examples include two dimensional simulations for a sample with a single notch under uniaxial tension, sample with a single notch under pure shear, sample with an asymmetric double notch under uniaxial tension, and finishing the section with three-dimensional dog-bone shaped sample and cylindrical shell under uniaxial tension. The load vs displacement curves, dissipated energies, relative mass density contours, and crack paths are determined. All numerical examples are conducted within the finite-element framework, where the two-dimensional and three-dimensional domains are discretized using 4-node quadrilateral elements and 8-node linear bricks, respectively. Specifically, the adopted strain energy function is defined as follows

$$W = \frac{1}{2} k_{\text{bulk}} (J-1)^2 + c_1 \left(I_1' - 3\right) + c_2 \left(I_1' - 3\right)^2, \tag{49}$$

where I_1' is the first invariant of the distortional component of $\mathbf{C}$ (i.e. $I_1' = J^{-2/3}\mathbf{C}$), k_{bulk} is the bulk modulus, and $\{c_1, c_2\}$ are material parameters that control the distortional deformation.

In the present study, the material proprieties of abdominal aortic aneurysm were adopted. In particular, the uniaxial response of an abdominal aortic aneurysm[1] (AAA) material was fitted by Faye et al. [55] to the experimental data conducted by Raghavan et al. [61]. The material parameters of AAA that control the distortional deformation are $c_1 = 0.617$ MPa and $c_2 = 1.215$ MPa, the bulk modulus is $k_{\text{bulk}} = 500$ MPa, the energy limiter is $\Phi = 0.1686$ MPa [55,61], the sharpness parameter is $m = 10$, and the characteristic length is $l = 0.1$ mm. Substituting for Φ and m in (48) and evaluating the upper incomplete gamma function yields that the dissipated energy per unit depth for each failed element is given by

$$U_i = 0.95 A_i \Phi. \tag{50}$$

5.1. Single edge notched tensile sample

A square plate with a preexisting notch, subjected to uniaxial tension is presented in this example. The geometric setup and applied deformation are depicted in Fig. 3. In this example, a plane strain condition is assumed.[2] and the sample is assumed to have a preexisting notch at the left edge. In order to simulate the crack pattern precisely, the mesh is refined in the expected crack propagation path, i.e. in the middle right strip of the specimen.

The modeling is carried out on five unstructured meshes (i.e. the meshes have irregular patterns) differing in the element size with respect to the length scale parameter as reported in Table 1, where they are arranged from coarse to fine. The short notation M# is adopted to describe the element size in the different meshes. The notation characterizes the ratio of the characteristic length to the element size. For instance, the notation M3 corresponds to a mesh with a characteristic length that is three times the element size.

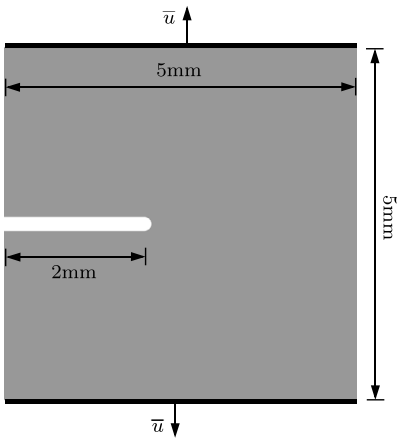

Fig. 3. Geometry and boundary conditions of single edge notched specimen under uniaxial tension.

The dissipated energy versus time is plotted in Fig. 4, where the total value of the dissipated energy for every mesh is tabulated in Table 1. It is noticed from Fig. 4 that the dissipated energy values are higher for the coarser meshes compared to the finer ones. Also, it can be seen that dissipated energy converges when refining the mesh and attains a constant value when the element size is at least one-ninth of the length scale parameter. It is worth mentioning that since the concept of time is dimensionless in quasi-static analysis, where the time is simply a pseudo-time, cracks in the various meshes may extend at different pseudo-time values involving dissipating energies at various pseudo-time scales. The latter reasoning implies normalizing the dissipated energies so they can be plotted on the same figure. Thus, in Fig. 4 the dissipated energies for all meshes are normalized with respect to time. Specifically, the parameter t_0 represents the pseudo-time at which the crack starts propagation and characterizes the beginning of energy dissipation through the creation of new crack surfaces. The parameter t_f represents the pseudo-time at which the crack reaches the end of the sample and characterizes the completion of the energy dissipation process.

Fig. 5 shows the total reaction force versus the applied displacement, where the maximum load on the load–displacement curve for every mesh is tabulated in Table 1. The results from the various meshes in Fig. 5 suggest that the load keeps increasing until reaching a maximum point followed by a sudden load drop, which is a signature of brittle fracture. On the other hand, it is noticed from comparing the results of the different meshes that the value of the maximum force on the load–displacement curve keeps decreasing under mesh refinement until reaching a threshold at which the maximum force attains a constant value. This threshold is noticed at an element size that is one-ninth of the length scale parameter. This finding is remarkable as most fracture modelings are conducted based on choosing the element size to be only one half of the length scale parameter.

Fig. 6a shows the progression of the relative mass density contours at different levels of loading with values ranging from 0 to 1, corresponding respectively to fully broken and intact states. Fig. 6b shows crack propagation, where elements having relative mass density less than or equal 10^{-6} at all their integration points are deleted. It is noticed that the crack propagates normal to the loading direction with a reasonably straight propagation path encompasses ups and downs resembling a real fracture. The crack path is in good agreement with the results of quasi-static brittle fracture available in the literature [37, 46,62–64] to name but a few.

[1] An abdominal aortic aneurysm (AAA) is a swelling in the aorta, which is the main artery that carries blood from the heart to the rest of the body.

[2] The B-matrix for plane strain element is presented in Appendix B

Table 1
Meshes' details for the single edge notched tensile sample. Also, the dissipated energies and maximum loads of single edge notched tensile sample for different meshes.

ID	Element size	Number of elements	Dissipated energy [Nmm/mm]	Maximum load [N/mm]
M3	$l/3$	4602	0.044	0.87
M5	$l/5$	10707	0.035	0.81
M7	$l/7$	20277	0.030	0.78
M9	$l/9$	32034	0.027	0.77
M10	$l/10$	38929	0.026	0.77

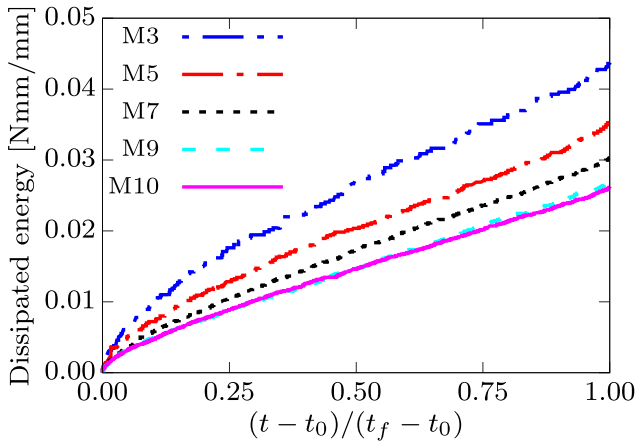

Fig. 4. Dissipated energy for single edge notched tensile sample for different meshes.

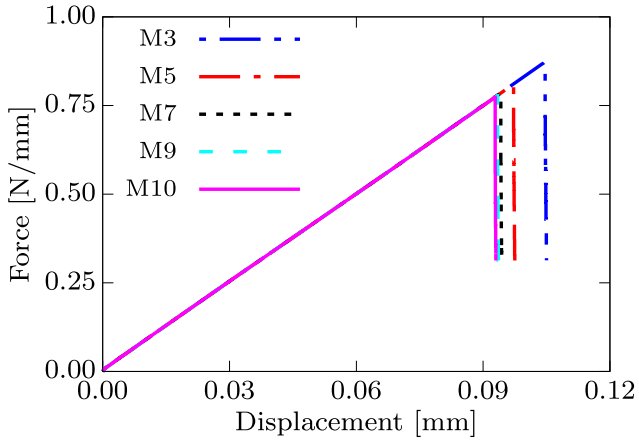

Fig. 5. Force vs displacement for single edge notched tensile sample for different meshes.

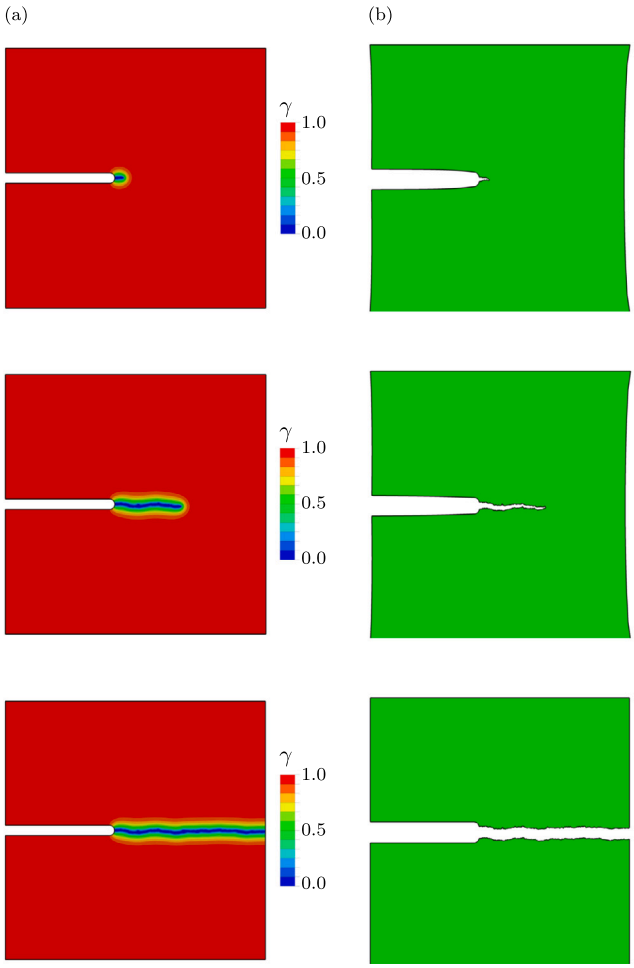

Fig. 6. Single edge notched tensile sample under different levels of remote tension. (a) Evolved relative mass density contours, and (b) evolved crack.

5.2. Single edge notched sample under pure shear

The problem considered throughout this section is the so-called shear test for a square sample with a preexisting notch as shown in Fig. 7. It is a well-known standard example in the literature on modeling of brittle fracture, see e.g. [37,65–68]. Specifically, the failure pattern in this test is not symmetric as a result of a non-trivial combination of local tension–compression and loading–unloading processes within the specimen during shear [69].

Here, the specimen is subjected to monotonic displacement that is imposed on the horizontal displacement of the top surface in a displacement-controlled quasi-static loading, while the vertical displacement of the same surface is constrained. On the other hand, both horizontal and vertical displacements of the bottom surface are fixed. The specimen domain is discretized by 31 165 unstructured linear quadrilateral reduced mixed finite elements. Fig. 8a shows the relative mass density contours and Fig. 8b shows the corresponding crack evolution, where elements satisfying deletion criterion are deleted. The results show that the crack initiates from the preexisting notch and propagates solely through the tensile part, where the crack is observed to kink down through the tensile region.

It is well-known in linear elasticity that the assumption of fracture driven by the total energy function (isotropic model) causes cracks to propagate in the areas under compression as shown in Fig. 9a, where two symmetric crack branches propagate, as was originally reported in [36]. Hence, different splits in the strain energy function have been proposed to restrict cracks to propagate only in the tensile regions. For example, Miehe et al. [37,38] suggested splitting the strain energy into tensile and compressive parts and applying degradation of only the tensile energy to avoid cracking in compression [68], see Fig. 9b. However, it is evident in Fig. 8 that the material-sink can model cracks to propagate only under tension naturally without any energy decomposition. This is due to the fact that the material-sink takes the

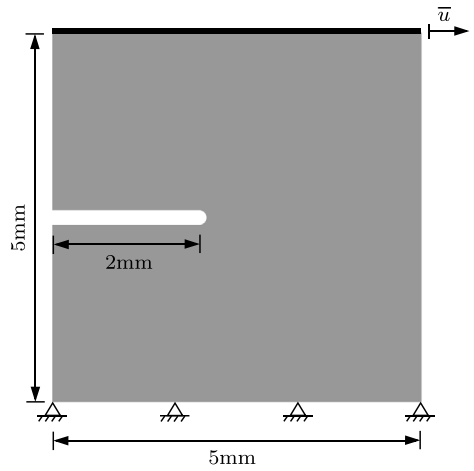

Fig. 7. Geometry and boundary conditions of single edge notched specimen under pure shear.

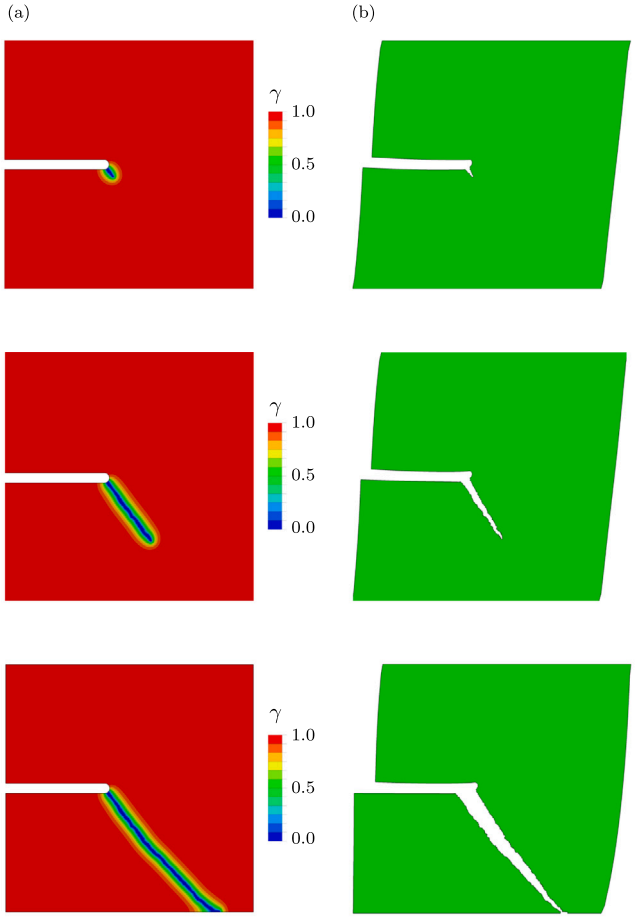

Fig. 8. Single edge notched sample under different levels of remote shear. (a) Relative mass density contours, and (b) crack propagation.

physics of the problem into account, where at large deformations; the tensile and compressive yield strengths are asymmetric.

5.3. Asymmetric double edge notched tensile sample

A square sample with asymmetric double notch, subjected to uniaxial tension is tested in this example as shown in Fig. 10. Plane Strain

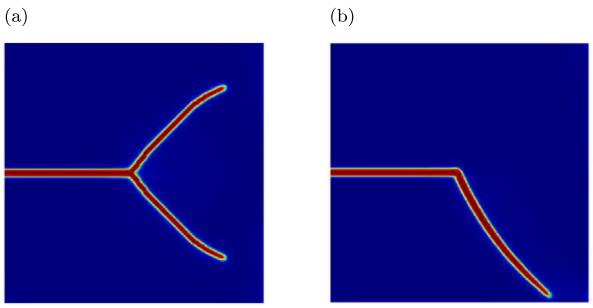

Fig. 9. Crack phase-field for single edge notched sample under pure shear [68]. (a) Isotropic model, and (b) Miehe et al. model [37,38].

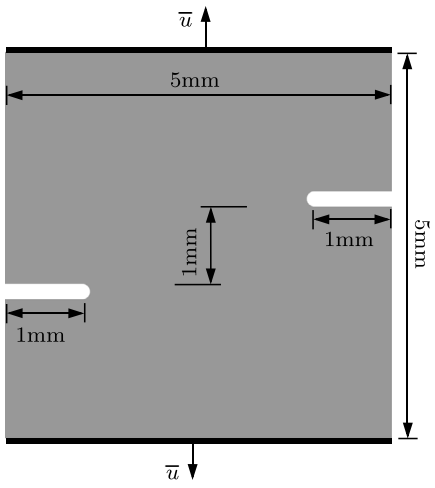

Fig. 10. Geometry and boundary conditions of the asymmetric double edge notched tensile sample.

condition is assumed, and all material parameters are as previously stated. The simulation is conducted on a structured mesh (i.e. the mesh has consistent pattern throughout the geometry) discretized with 53 988 linear quadrilateral reduced mixed finite elements as shown in Fig. 11a. The resulting relative mass density contours and crack propagation are shown in Fig. 11c and e respectively, where the bridging between the propagating cracks is noticed. The predicted crack path is in good agreement with results obtained by [62,63,70] to list but a few.

Additional simulation is also conducted using an unstructured distorted mesh and discretized with 34 784 linear quadrilateral reduced mixed finite elements as shown in Fig. 11b. The resulting relative mass density contours and crack propagation are shown in Fig. 11d and f respectively. The crack propagates from the top notch in a fairly straight line path, and when it approaches the end of the sample, it kinks down towards the bottom notch. The force versus displacement responses for both meshes are shown in Fig. 12, where it is noticed that the maximum force at which the sample fails is almost the same for both meshes.

It is apparent in the case of unstructured mesh that the crack may propagate from the bottom or the top notch because of numerical inhomogeneities resulting from the unstructured mesh. It is worth noting that imperfections in material (e.g. defects, voids, etc.) can act in the same way as the unstructured mesh (mesh inhomogeneities) leading the crack to propagate from the weakest notch, and once it propagates from one notch, it is highly expected to propagate further in the same path relieving the other notch.

The results in Fig. 11c and d may also indicate a weak mesh dependence, see Faye et al. [55]. However, the latter hypothesis may be refuted based on the fact that for all other models (e.g. single edge

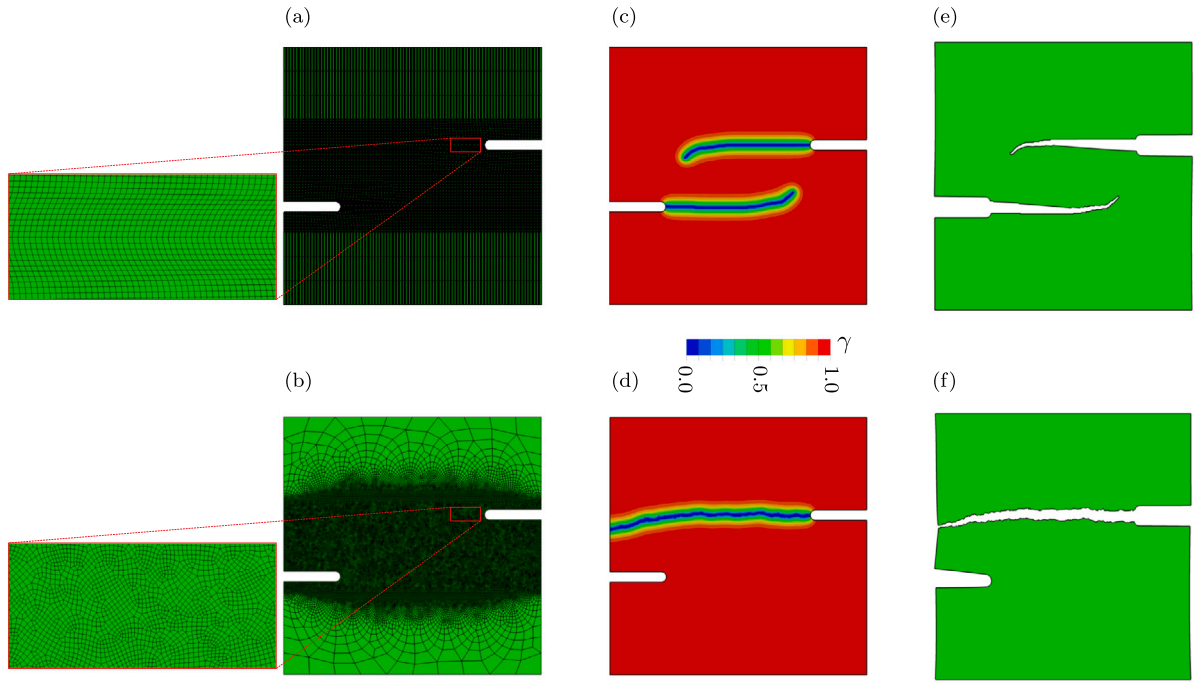

Fig. 11. Meshes discretization for the asymmetric double edge notched sample showing the (**a**) structured mesh and (**b**) unstructured mesh. Evolved relative mass density of (**c**) structured mesh and (**d**) unstructured mesh. Crack propagation of (**e**) structured mesh and (**f**) unstructured mesh.

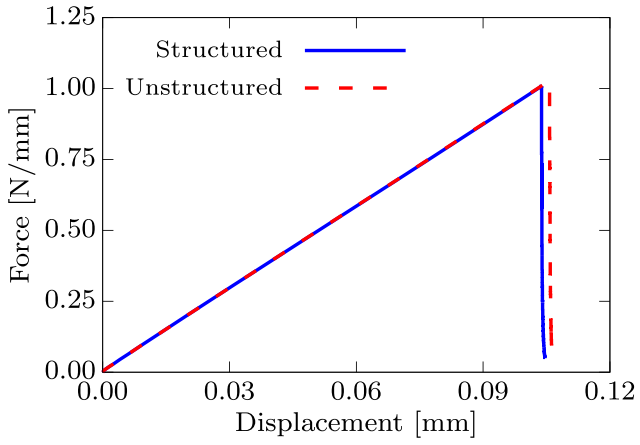

Fig. 12. Force vs displacement for the asymmetric double edge notched sample for both the structured and unstructured meshes.

notched sample under tension, single edge notched sample under pure shear), various meshes have been used and all of them lead to the same crack patterns.

5.4. Three-dimensional dog-bone shaped sample

A three-dimensional dog-bone shaped specimen, subjected to uniaxial tension is examined in this subsection. The simulations are conducted on two dog-bone shaped samples, DB1 and DB2. The samples' geometric properties and boundary conditions are depicted in Fig. 13. DB1 is a dog-bone shaped specimen with rectangular grip sections, a rectangular narrow section, and four fillets connecting the two grip sections with the narrow section. On the other hand, DB2 is identical to DB1, whereas its narrow section incorporates a small imperfection introduced by two small arcs. The thickness of both samples is 0.2 mm. The two samples are subjected to monotonic displacement that is imposed on the vertical displacement of the top and bottom surfaces in a displacement-controlled quasi-static loading, while the specimens' domains are discretized by 17 242 and 18 691 unstructured bricks respectively.

Fig. 14 shows the strain energy contours for both samples just prior crack propagation, where locations of the maximum strain energies are different in both cases. In the DB1 case, the maximum energy is located at the top right intersection point between the fillet and the narrow section, while in the DB2 case, the maximum energy is located at the left mid-height distance of the sample. Fig. 15a, b, and c show crack propagation for DB1 under different levels of remote tension, while Fig. 15d, e, and f show crack propagation for DB2 under different levels of remote tension. With increasing load, the crack initiates and propagates from the intersection point between the fillet and the sample's narrow section in DB1. On the other hand, in DB2 the crack propagates at the middle height of the sample followed by a complete fracture of the specimen into two halves. The results demonstrate the high capabilities of the MS approach to model cracks in three-dimensional solids, where the material-sink modeling in 2D and 3D solids is done exactly in the same way.

Furthermore, crack initiation and propagation in DB1 from the intersection point between the narrow section and the fillet indicates that the MS is attentive to the physics of the problem that is being modeled, where the crack propagates at the place of abrupt change of the section, which acts as a local, micro stress concentrator. That is to say, the results suggest that the place at which the crack is first noticed may be widely affected by small imperfections presented in the geometry.

Fig. 16 shows the force versus displacement responses for both samples. One can notice that the load keeps increasing until reaching a maximum point followed by load drop, where the maximum force at which failure occurs is almost identical for both DB1 and DB2 samples. The latter observation is noteworthy since it implies that the

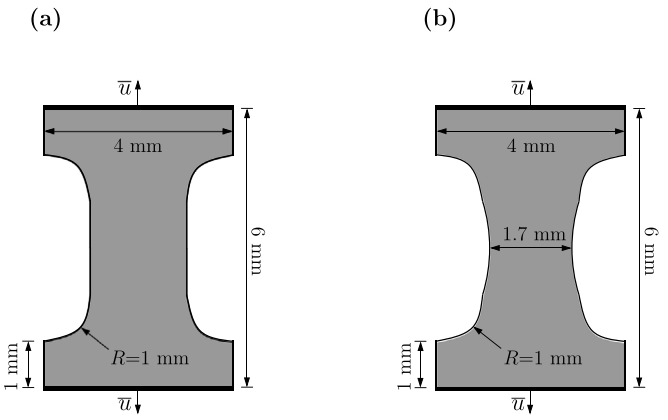

Fig. 13. Geometry and boundary conditions of the three-dimensional dog bone shaped samples. (a) DB1 and (b) DB2. DB1 has a rectangular stem with constant stem width; DB2 has a small imperfection introduced by an arc in the stem. The thickness of both samples is 0.2 mm.

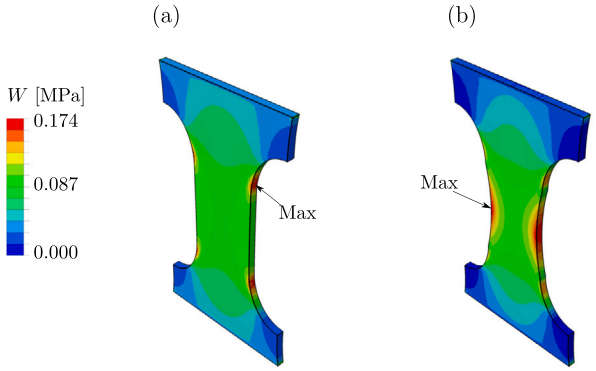

Fig. 14. Strain energy contours of dog-bone shaped specimen just before crack propagation for (a) DB1 and (b) DB2.

loads at which the samples fail are almost the same, however, the cracks propagate from different locations in each case induced by small imperfections taking place in the sample's geometry.

5.5. Cylindrical shell

Finally, the MS method is examined using an initially curved structure. In particular, since the material under consideration is AAA material, an artery-like sample is examined in this subsection. The sample is a thin-walled cylinder made of AAA material resembling a real artery under uniaxial tension with an initial through-thickness notch. Owing to the problem symmetry, only the quarter of the full shell is analyzed as shown in Fig. 17a.

Specifically, the outer and inner diameters of the sample are 5.0 mm and 4.6 mm, respectively. The notch is half a circle with a diameter of 0.4 mm. Regarding the supporting conditions, the right edge is fully clamped, while the left edge is subjected to a displacement controlled quasi-static tensile loading in the axial direction, while the specimen is subjected to symmetric boundary conditions.

Fig. 17b and c show the evolution of the relative mass density contours at different loading stages until complete fracture of the specimen. The crack initiates from the initial notch and propagates in a curved path that is perpendicular to the direction of the tensile loading, where the crack perfectly follows the Mode I crack direction along the cylindrical shape.

The results show the ability of the MS to simulate crack initiation and propagation in curved geometries, where it predicts cracks in an arbitrary topological complexity — without the need for any ad hoc criteria.

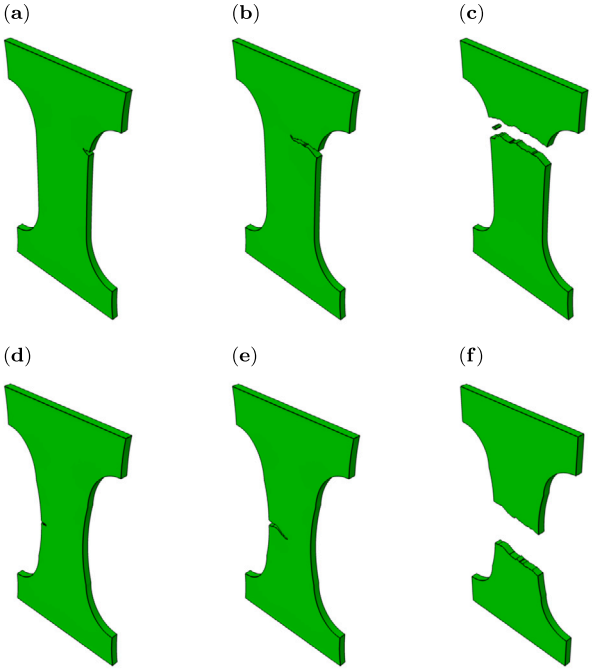

Fig. 15. Crack propagation in the dog-bone shaped specimens under different levels of remote tension. (a), (b) and (c) for DB1 sample; (d), (e), and (f) for DB2 sample.

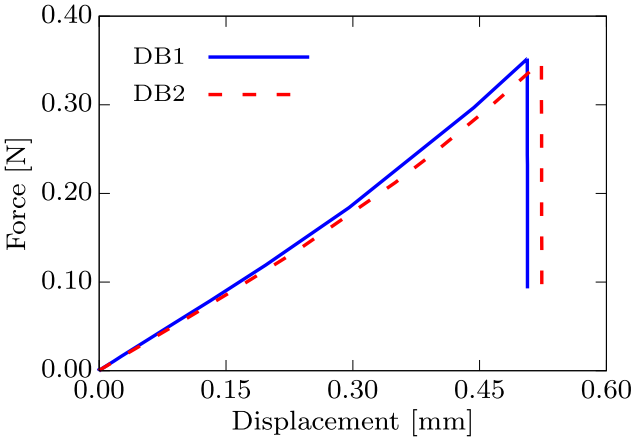

Fig. 16. Force vs displacement for the dog-bone shaped specimens.

6. Conclusions

A modified version of the MS approach is developed in the present study implemented in Abaqus/Standard 2020 using the user elements utility. The MS approach is a physics-based approach, which is inspired by the fact that the crack process leads to local loss of material. The latter implies that the mass balance shall be coupled with momenta balance. Thus, the whole fracture process is embedded within the partial differential equations (i.e. mass and momenta balance) leading to propagate cracks in a spontaneous manner. On the other hand, the mass balance equation presents the mass density as the damage variable that decreases in the damaged areas indicating where the crack will take place. The developed finite element is based on the reduced

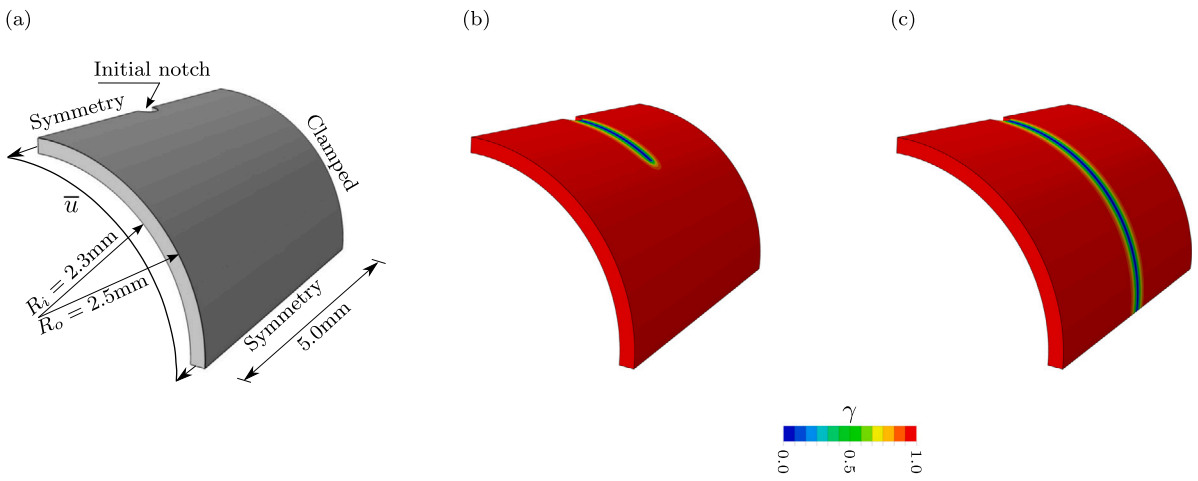

Fig. 17. (**a**) Geometry and loading conditions of tensile test of a cylindrical shell; (**b**) and (**c**) relative mass density contours at different levels of remote tension.

mixed finite-element formulation with displacements and relative mass density degrees of freedom.

Numerical examples included a single edge notched sample under uniaxial tension discretized with unstructured meshes which highlighted the fact that the element size shall be at least one-ninth of the length scale parameter to ensure convergence of the dissipated energy presenting a new insight into the common practice of choosing the element size to be only one half the length scale parameter. A single edge notched sample under pure shear has been used to test the theory for the combination of tension–compression processes. It is notably that the crack propagated only in the tension part without the need to any energy decomposition, which emphasizes the fact of asymmetry of failure in tension and compression in the case of large deformations. Other examples including two-dimensional asymmetric double edge notched square sample, three-dimensional dog-bone shaped sample and cylindrical shell with initial notch have demonstrated the capability of the MS approach in modeling complex crack patterns.

CRediT authorship contribution statement

Suhib Abu-Qbeitah: Software and program for simulations, Validation, Numerical simulations, Writing – original draft. **Mahmood Jabareen:** Conceptualization, Methodology, Formulation and program for simulations, Validation, Writing – review & editing, Project administration. **Konstantin Y. Volokh:** Conceptualization, Methodology, Writing – review & editing, Project administration, Funding acquisition.

Declaration of competing interest

The authors declare that they have no known competing financial interests or personal relationships that could have appeared to influence the work reported in this paper.

Data availability

Data will be made available on request.

Acknowledgments

The support from the Israel Science Foundation, Israel (ISF-394/20) is gratefully acknowledged. Also, M. Jabareen is supported by Neubauer Foundation.

Appendix A. Derivation of the geometrical stiffness matrix

To develop the geometrical tangent stiffness matrix the multiplication $\overline{\mathbf{S}} : \Delta\delta\overline{\mathbf{E}}$ should be written in matrix form

$$\begin{aligned}\overline{\mathbf{S}} : \Delta\delta\overline{\mathbf{E}} = \frac{1}{2}\left(\frac{\overline{J}}{J}\right)^{2/3}\left(\overline{\mathbf{S}} : \Delta\delta\mathbf{C}\right) \\ + \frac{1}{3}\left(\frac{\Delta\overline{J}}{\overline{J}} - \frac{\Delta J}{J}\right)\left(\overline{\mathbf{S}} : \delta\overline{\mathbf{C}}\right) \\ + \frac{1}{3}\left(\frac{\delta\overline{J}}{\overline{J}} - \frac{\delta J}{J}\right)\left(\overline{\mathbf{S}} : \Delta\overline{\mathbf{C}}\right) \\ + \frac{1}{3}\left(\frac{\Delta\delta\overline{J}}{\overline{J}} - \frac{\Delta\delta J}{J} - \frac{5}{3}\frac{\Delta\overline{J}\delta\overline{J}}{\overline{J}^2} + \frac{1}{3}\frac{\delta J\Delta J}{J^2}\right. \\ \left. + \frac{2}{3}\frac{\Delta J}{J}\frac{\delta\overline{J}}{\overline{J}} + \frac{2}{3}\frac{\Delta\overline{J}}{\overline{J}}\frac{\delta J}{J}\right)\left(\overline{\mathbf{S}} : \overline{\mathbf{C}}\right).\end{aligned} \tag{51}$$

The term $\frac{1}{2}\left(\overline{\mathbf{S}} : \Delta\delta\mathbf{C}\right)$ in (51) can be rewritten using the linearization of the variation of the right Cauchy–Green deformation tensor $\Delta\delta\mathbf{C} = \delta\mathbf{F}^{\mathrm{T}}\Delta\mathbf{F} + \Delta\mathbf{F}^{\mathrm{T}}\delta\mathbf{F}$ as follows

$$\frac{1}{2}\left(\overline{\mathbf{S}} : \Delta\delta\mathbf{C}\right) = \delta\hat{\underline{\mathbf{u}}}^{\mathrm{T}}\underline{\underline{\mathbf{k}}}_G\Delta\hat{\underline{\mathbf{u}}}, \tag{52}$$

where the matrix $\underline{\underline{\mathbf{k}}}_G$ is defined by

$$\underline{\underline{\mathbf{k}}}_G = \begin{bmatrix} \underline{\underline{\mathbf{G}}}_{11} & \underline{\underline{\mathbf{G}}}_{12} & \cdots & \underline{\underline{\mathbf{G}}}_{18} \\ \underline{\underline{\mathbf{G}}}_{21} & \underline{\underline{\mathbf{G}}}_{22} & \cdots & \underline{\underline{\mathbf{G}}}_{28} \\ \vdots & \vdots & \ddots & \vdots \\ \underline{\underline{\mathbf{G}}}_{81} & \underline{\underline{\mathbf{G}}}_{82} & \cdots & \underline{\underline{\mathbf{G}}}_{88} \end{bmatrix}, \tag{53}$$

and the sub-matrices $\underline{\underline{\mathbf{G}}}_{IJ}$ are given by

$$\underline{\underline{\mathbf{G}}}_{IJ} = \left(\sum_{i=1}^{3}\sum_{j=1}^{3}\frac{\partial N_I}{\partial X_i}\overline{S}_{ij}\frac{\partial N_J}{\partial X_j}\right)\underline{\underline{\mathbf{I}}}. \tag{54}$$

In (54) $\underline{\underline{\mathbf{I}}}$ is the 3 × 3 identity matrix. Also, the third term of the linearization of the variation of the volume change given in ((30)a) can be rewritten in a similar manner as the multiplication in (52)

$$\frac{1}{2}\mathbf{C}^{-1} : \Delta\delta\mathbf{C} = \delta\hat{\underline{\mathbf{u}}}^{\mathrm{T}}\underline{\underline{\mathbf{g}}}_C\Delta\hat{\underline{\mathbf{u}}}, \tag{55}$$

where the matrix $\underline{\underline{\mathbf{g}}}_C$ is defined by

$$\underline{\underline{\mathbf{g}}}_C = \begin{bmatrix} \underline{\underline{\mathbf{G}}}^C_{11} & \underline{\underline{\mathbf{G}}}^C_{12} & \cdots & \underline{\underline{\mathbf{G}}}^C_{18} \\ \underline{\underline{\mathbf{G}}}^C_{21} & \underline{\underline{\mathbf{G}}}^C_{22} & \cdots & \underline{\underline{\mathbf{G}}}^C_{28} \\ \vdots & \vdots & \ddots & \vdots \\ \underline{\underline{\mathbf{G}}}^C_{81} & \underline{\underline{\mathbf{G}}}^C_{82} & \cdots & \underline{\underline{\mathbf{G}}}^C_{88} \end{bmatrix}, \tag{56}$$

and the sub-matrices $\underline{\underline{\mathbf{G}}}^{C}_{IJ}$ are given by

$$\underline{\underline{\mathbf{G}}}^{C}_{IJ} = \left(\sum_{i=1}^{3} \sum_{j=1}^{3} \frac{\partial N_I}{\partial X_i} C^{-1}_{ij} \frac{\partial N_J}{\partial X_j} \right) \underline{\underline{\mathbf{I}}}. \tag{57}$$

Using the relationship $\Delta\mathbf{C}^{-1} = -\mathbf{C}^{-1}\Delta\mathbf{C}\mathbf{C}^{-1}$, the second term in ((30)a) can be rewritten as follows

$$\begin{aligned} \frac{1}{2} J\delta\mathbf{C} : \Delta\mathbf{C}^{-1} &= \frac{1}{2} J\delta\mathbf{C} : \left(\mathbf{C}^{-1} \odot \mathbf{C}^{-1}\right) : \Delta\mathbf{C} \\ &= \delta\underline{\hat{\mathbf{u}}}^{\mathrm{T}} \left[J \underline{\underline{\mathbf{B}}}^{\mathrm{T}}_{u} \underline{\underline{\mathbf{D}}}_{C} \underline{\underline{\mathbf{B}}}_{u} \right] \Delta\underline{\hat{\mathbf{u}}}, \end{aligned} \tag{58}$$

where the tensor product $\odot$ and the matrix $\underline{\underline{\mathbf{D}}}_{C}$ are defined as follows accordingly

$$(\mathbf{A} \odot \mathbf{B})_{ijkl} = \frac{1}{2} \left(A_{ik} B_{jl} + A_{il} B_{jk} \right), \tag{59}$$

$$\underline{\underline{\mathbf{D}}}_{C} = \mathrm{Voigt}\left(2\mathbf{C}^{-1} \odot \mathbf{C}^{-1}\right). \tag{60}$$

Thus, the linearization of the variation of the volume change given in ((30)a) can be expressed as follows

$$\Delta\delta J = \delta\underline{\hat{\mathbf{u}}}^{\mathrm{T}} \underline{\mathbf{a}}_{2} \Delta\underline{\hat{\mathbf{u}}}, \quad \underline{\mathbf{a}}_{2} = \frac{\mathbf{a}_1^{\mathrm{T}}\mathbf{a}_1}{J} - J \underline{\underline{\mathbf{B}}}^{\mathrm{T}}_{u} \underline{\underline{\mathbf{D}}}_{C} \underline{\underline{\mathbf{B}}}_{u} + J\underline{\mathbf{g}}_{C}, \tag{61}$$

and volume of average of $\Delta\delta J$ is given by

$$\Delta\delta\overline{J} = \delta\underline{\hat{\mathbf{u}}}^{\mathrm{T}} \overline{\underline{\mathbf{a}}}_{2} \Delta\underline{\hat{\mathbf{u}}}, \quad \overline{\underline{\mathbf{a}}}_{2} = \frac{1}{\Omega^{\mathrm{e}}_0} \int_{\Omega^{\mathrm{e}}_0} \underline{\mathbf{a}}_{2} \, d\Omega^{\mathrm{e}}_0. \tag{62}$$

Finally, using the results in (34), (37), (52), (55), (61) and (62), the multiplication $\overline{\mathbf{S}} : \Delta\delta\overline{\mathbf{E}}$ in (51) is simplified as follows

$$\overline{\mathbf{S}} : \Delta\delta\overline{\mathbf{E}} = \delta\underline{\hat{\mathbf{u}}}^{\mathrm{T}} \overline{\underline{\mathbf{k}}}_{G} \Delta\underline{\hat{\mathbf{u}}}, \tag{63}$$

where the geometrical stiffness matrix $\overline{\underline{\mathbf{k}}}_{G}$ is given by

$$\begin{aligned} \overline{\underline{\mathbf{k}}}_{G} &= \left(\frac{\overline{J}}{J}\right)^{2/3} \underline{\mathbf{k}}_{G} + \frac{2}{3} \left(\frac{\overline{\underline{\mathbf{a}}}_1}{\overline{J}} - \frac{\underline{\mathbf{a}}_1}{J} \right) \underline{\overline{\mathbf{S}}}^{\mathrm{T}} \underline{\underline{\mathbf{B}}}_{u} \\ &+ \frac{2}{3} \underline{\underline{\mathbf{B}}}^{\mathrm{T}}_{u} \underline{\overline{\mathbf{S}}} \left(\frac{\overline{\underline{\mathbf{a}}}_1^{\mathrm{T}}}{\overline{J}} - \frac{\underline{\mathbf{a}}_1^{\mathrm{T}}}{J} \right) \\ &+ \frac{1}{3} \left(\overline{\mathbf{S}} : \overline{\mathbf{C}} \right) \left(\frac{\overline{\underline{\mathbf{a}}}_2}{\overline{J}} - \frac{\underline{\mathbf{a}}_2}{J} - \frac{5}{3} \frac{\overline{\underline{\mathbf{a}}}_1 \overline{\underline{\mathbf{a}}}_1^{\mathrm{T}}}{\overline{J}^2} + \frac{1}{3} \frac{\underline{\mathbf{a}}_1 \underline{\mathbf{a}}_1^{\mathrm{T}}}{J^2} \right. \\ &\left. + \frac{2}{3} \frac{\overline{\underline{\mathbf{a}}}_1 \underline{\mathbf{a}}_1^{\mathrm{T}}}{\overline{J} J} + \frac{2}{3} \frac{\underline{\mathbf{a}}_1 \overline{\underline{\mathbf{a}}}_1^{\mathrm{T}}}{J \overline{J}} \right). \end{aligned} \tag{64}$$

Appendix B. 2D elements

For a plane-strain element 2D element the following components of the deformation gradient $F_{13} = F_{31} = F_{23} = F_{32} = 0$ vanish while $F_{33} = 1$. Likewise, the matrix $\underline{\underline{\mathbf{B}}}_{u}$ is of size 4×8 that consists of four sub-matrices $\underline{\underline{\mathbf{B}}}_{I}$. Each sub-matrix $\underline{\underline{\mathbf{B}}}_{I}$ is of size 4×2 and has the following form

$$\underline{\underline{\mathbf{B}}}_{I} = \begin{bmatrix} F_{11} N_{I,1} & F_{21} N_{I,1} \\ F_{12} N_{I,2} & F_{22} N_{I,2} \\ 0 & 0 \\ F_{11} N_{I,2} + F_{12} N_{I,1} & F_{21} N_{I,2} + F_{22} N_{I,1} \end{bmatrix}. \tag{65}$$

The column vector consisting of the components of the inverse of the right Cauchy–Green deformation tensor is defined as

$$\underline{\mathbf{C}}^{-1} = \left\{ C^{-1}_{11}, C^{-1}_{22}, C^{-1}_{33}, C^{-1}_{12} \right\}^{\mathrm{T}}, \tag{66}$$

and, the second Piola–Kirchhoff stress vector is given by

$$\underline{\overline{\mathbf{S}}} = \left\{ \overline{S}_{11}, \overline{S}_{22}, \overline{S}_{33}, \overline{S}_{12} \right\}^{\mathrm{T}}. \tag{67}$$

References

[1] Griffith AA. The phenomena of rupture and flow in solids. Philos Trans R Soc Lond Ser A Math Phys Eng Sci 1921;221(582–593):163–98.
[2] Elishakoff I, Volokh KY. Centenary of two pioneering theories in mechanics. Math Mech Solids 2021.
[3] Irwin GR. Fracture. Berlin, Heidelberg: Springer Berlin Heidelberg; 1958, p. 551–90.
[4] Barenblatt GI. The formation of equilibrium cracks during brittle fracture. General ideas and hypotheses. Axially-symmetric cracks. J Appl Math Mech 1959;23:622–36.
[5] Needleman A. A continuum model for void nucleation by inclusion debonding. J Appl Mech 1987;54:525–31.
[6] Rice JR, Wang J-S. Embrittlement of interfaces by solute segregation. Mater Sci Eng A 1989;107:23–40.
[7] Tvergaard V, Hutchinson JW. The relation between crack growth resistance and fracture process parameters in elastic-plastic solids. J Mech Phys Solids 1992;40:1377–97.
[8] Camacho GT, Ortiz M. Computational modelling of impact damage in brittle materials. Int J Solids Struct 1996;33:2899–938.
[9] de Borst R. Some recent issues in computational failure mechanics. Internat J Numer Methods Engrg 2001;52:63–95.
[10] Xu XP, Needleman A. Numerical simulations of fast crack growth in brittle solids. J Mech Phys Solids 1994;42:1397–434.
[11] Moes N, Dolbow J, Belytschko T. A finite element method for crack growth without remeshing. Internat J Numer Methods Engrg 1999;46:131–50.
[12] Zhou F, Molinari JF. Dynamic crack propagation with cohesive elements: A methodology to address mesh dependency. Internat J Numer Methods Engrg 2004;59(1):1–24.
[13] Azevedo NM, Lemos J. Hybrid discrete element/finite element method for fracture analysis. Comput Methods Appl Mech Engrg 2006;195(33–36):4579–93.
[14] Park K, Paulino GH, Roesler JR. A unified potential-based cohesive model of mixed-mode fracture. J Mech Phys Solids 2009;57:891–908.
[15] Peng GL, Wang YH. A node split method for crack growth problem. Appl Mech Mater 2012;(182–183):1524–8.
[16] Gong B, Paggi M, Carpinteri A. A cohesive crack model coupled with damage for interface fatigue problems. Int J Fract 2012;137:91–104.
[17] Msekh MA, Sargado JM, Jamshidian M, Areias PM, Rabczuk T. Abaqus implementation of phase-field model for brittle fracture. Comput Mater Sci 2015;96:472–84.
[18] Rabczuk T. Computational methods for fracture in brittle and quasi-brittle solids: State-of-the-art review and future perspectives. ISRN Appl Math 2013;3.
[19] Nikolic M, Do XN, Ibrahimbegovic A, Nikolic Z. Crack propagation in dynamics by embedded strong discontinuity approach: Enhanced solid versus discrete lattice model. Comput Methods Appl Mech Engrg 2018;340:480–99.
[20] Manzoli O, Shing P. A general technique to embed non-uniform discontinuities into standard solid finite elements. Comput Struct 2006;84:742–57.
[21] Moes N, Gravouil A, Belytschko T. Non-planar 3D crack growth by the extended finite element and level sets-part i: Mechanical model. Internat J Numer Methods Engrg 2002;53:2549–68.
[22] Kachanov LM. Time of the rupture process under creep conditions. Izv Akad Nauk SSSR 1958;8:26–31, Otdelenie Teckhnicheskikh Nauk.
[23] Gurson AL. Continuum theory of ductile rupture by void nucleation and growth: Part I-yield criteria and flow rules for porous ductile media. J Eng Mater Technol 1977;99:2–15.
[24] Voyiadjis GZ, Kattan PI. A plasticity-damage theory for large deformation of solids—I. Theoretical formulation. Internat J Engrg Sci 1992;30:1089–108.
[25] Gao H, Klein P. Numerical simulation of crack growth in an isotropic solid with randomized internal cohesive bonds. J Mech Phys Solids 1998;46:187–218.
[26] Klein P, Gao H. Crack nucleation and growth as strain localization in a virtual-bond continuum. Eng Fract Mech 1998;61:21–48.
[27] Lemaitre J, Desmorat R. Engineering damage mechanics: ductile, creep, fatigue and brittle failures. Berlin: Springer; 2005.
[28] Volokh KY. Nonlinear elasticity for modeling fracture of isotropic brittle solids. J Appl Mech 2004;71:141–3.
[29] Benzerga AA, Leblond JB, Needleman A, Tvergaard V. Ductile failure modeling. Int J Fract 2016;201:29–80.
[30] Pijaudier-Cabot G, Bažant Z. Nonlocal damage theory. J Eng Mech 1987;113:1512–33.
[31] Lasry D, Belytschko T. Localization limiters in transient problems. Int J Solids Struct 1988;24:581–97.
[32] Peerlings RHJ, de Borst R, Brekelmans WAM, de Vree JHP. Gradient enhanced damage for quasi-brittle materials. Internat J Numer Methods Engrg 1996;39:3391–403.
[33] de Borst R, van der Giessen E. Material instabilities in solids. Chichester: Wiley; 1998.
[34] Silling SA. Reformulation of elasticity theory for discontinuities and long-range forces. J Mech Phys Solids 2000;48:175–209.
[35] Francfort GA, Marigo JJ. Revisiting brittle fracture as an energy minimization problem. J Mech Phys Solids 1998;46:1319–42.

[36] Bourdin B, Francfort GA, Marigo JJ. Numerical experiments in revisited brittle fracture. J Mech Phys Solids 2000;48:797–826.
[37] Miehe C, Hofacker M, Welschinger F. A phase field model for rate-independent crack propagation: Robust algorithmic implementation based on operator splits. Comput Methods Appl Mech Engrg 2010;199:2765–78.
[38] Miehe C, Welschinger F, Hofacker M. Thermodynamically consistent phase-field models of fracture: Variational principles and multi-field FE implementations. Internat J Numer Methods Engrg 2010;83:1273–311.
[39] Hofacker M, Miehe C. A phase field model of dynamic fracture: Robust field updates for the analysis of complex crack patterns. Internat J Numer Methods Engrg 2012;93:276–301.
[40] Hofacker M, Miehe C. Continuum phase field modeling of dynamic fracture: Variational principles and staggered FE implementation. Int J Fract 2012;178:113–29.
[41] Borden MJ, Verhoosel CV, Scott MA, Hughes TJR, Landis CM. A phase-field description of dynamic brittle fracture. Comput Methods Appl Mech Engrg 2012;217–220:77–95.
[42] Liu G, Li Q, Msekh MA, Zuo Z. Abaqus implementation of monolithic and staggered schemes for quasi-static and dynamic fracture phase-field model. Comput Mater Sci 2016;121:35–47.
[43] Miehe C, Schänzel L-M. Phase field modeling of fracture in rubbery polymers. part i: Finite elasticity coupled with brittle failure. J Mech Phys Solids 2014;65:93–113.
[44] Raina A, Miehe C. A phase-field model for fracture in biological tissues. Biomech Model Mechanobiol 2016;15:479–96.
[45] Miehe C, Aldakheel F, Raina A. Phase field modeling of ductile fracture at finite strains: A variational gradient-extended plasticity-damage theory. Int J Plast 2016;84:1–32.
[46] Wu JY, Huang Y. Comprehensive implementations of phase-field damage models in abaqus. Theor Appl Fract Mech 2020;106:102440.
[47] Russ J, Slesarenko V, Rudykh S, Waisman H. Rupture of 3D-printed hyperelastic composites: Experiments and phase field fracture modeling. J Mech Phys Solids 2020;140:103941.
[48] Volokh KY. Fracture as a material sink. Mater Theory 2017;1(3).
[49] Volokh KY. Hyperelasticity with softening for modeling materials failure. J Mech Phys Solids 2007;55:2237–64.
[50] Volokh KY. On modeling failure of rubber-like materials. Mech Res Commun 2010;37:684–9.
[51] Volokh KY. Characteristic length of damage localization in rubber. Int J Fract 2011;168:113–6.
[52] Volokh KY. Review of the energy limiters approach to modeling failure of rubber. Rubber Chem Technol 2013;86(3):470–87.
[53] Volokh KY. Characteristic length of damage localization in concrete. Mech Res Commun 2013;51:29–31.
[54] Volokh KY. Mechanics of soft materials. 2nd ed.. Singapore: Springer; 2019.
[55] Faye A, Lev Y, Volokh KY. The effect of local inertia around the crack-tip in dynamic fracture of soft materials. Mech Soft Mater 2019.
[56] Abaqus/Standard. 2020, Dassault Systemes Simulia Corp., Johnston, RI, USA.
[57] Volokh KY. New approaches to modeling failure and fracture of rubber-like materials. In: Fatigue crack growth in rubber materials. Adv Polym Sci 2021;286:131–52.
[58] Jabareen M. A polygonal finite element formulation for modeling nearly incompressible materials. Meccanica 2020;55:701–23.
[59] Bishara D, Jabareen M. A reduced mixed finite-elementformulation for modeling the viscoelastic response of electro-active polymers at finite deformation. Math Mech Solids 2018;24(5):1578–610.
[60] Chester SA, Leo CVD, Anand L. A finite element implementation of a coupled diffusion-deformation theory for elastomeric gels. Int J Solids Struct 2015;52:1–18.
[61] Raghavan ML, Vorp DA. Toward a biomechanical tool to evaluate rupture potential of abdominal aortic aneurysm: Identification of a finite strain constitutive model and evaluation of its applicability. J Biomech 2000;33:475–82.
[62] Bhowmick S, Liu GR. A phase-field modeling for brittle fracture and crack propagation based on the cell-based smoothed finite element method. Eng Fract Mech 2018;204:369–87.
[63] Molnar G, Gravouil A. 2D and 3D abaqus implementation of a robust staggered phase-field solution for modeling brittle fracture. Finite Elem Anal Des 2017;130:27–38.
[64] Seles K, Lesicar T, Tonkovic Z, Soric J. A residual control staggered solution scheme for the phase-field modeling of brittle fracture. Eng Fract Mech 2019;205:370–86.
[65] Borden MJ, Hughes TJR, Landis CM, Verhoosel CV. A higher-order phase-field model for brittle fracture: Formulation and analysis within the isogeometric analysis framework. Comput Methods Appl Mech Engrg 2014.
[66] Vignollet J, May S, de Borst R, Verhoosel CV. Phase-field models for brittle and cohesive fracture. Meccanica 2014;49:2587–601.
[67] Heister T, Wheeler MF, Wick T. A primal–dual active active set method and predictor–corrector mesh adaptivity for computing fracture propagation using a phase-field approach. Comput Methods Appl Mech Engrg 2015;290:466–95.
[68] Ambati M, Gerasimov T, Lorenzis LD. A review on phase-field models of brittle fracture and a new fast hybrid formulation. Comput Mech 2015;55:383–405.
[69] Gerasimov T, Lorenzis LD. A line search assisted monolithic approach for phase-field computing of brittle fracture. Comput Methods Appl Mech Engrg 2016;312:276–303.
[70] Hirshikesh H, Pramod A, Waisman H, Natarajan S. Adaptive phase field method using novel physics based refinement criteria. Comput Methods Appl Mech Engrg 2021;383:113874.